1-1-2017

Anisotropic Character of Low-Order Turbulent Flow Descriptions Through the Proper Orthogonal Decomposition

Nicholas Hamilton
Portland State University

Murat Tutkun
University of Oslo

Raúl Bayoán Cal
Portland State Universty, rcal@pdx.edu

Citation Details

Anisotropic character of low-order turbulent flow descriptions through the proper orthogonal decomposition

Nicholas Hamilton,[1] Murat Tutkun,[2,3] and Raúl Bayoán Cal[1]

[1]*Department of Mechanical and Materials Engineering, Portland State University, Portland, Oregon 97202, USA*
[2]*Department of Process and Fluid Flow Technology, IFE, 2007 Kjeller, Norway*
[3]*Department of Mathematics, University of Oslo, Blindern, 0316 Oslo, Norway*

Proper orthogonal decomposition (POD) is applied to distinct data sets in order to characterize the propagation of error arising from basis truncation in the description of turbulence. Experimental data from stereo particle image velocimetry measurements in a wind turbine array and direct numerical simulation data from a fully developed channel flow are used to illustrate dependence of the anisotropy tensor invariants as a function of POD modes used in low-order descriptions. In all cases, ensembles of snapshots illuminate a variety of anisotropic states of turbulence. In the near wake of a model wind turbine, the turbulence field reflects the periodic interaction between the incoming flow and rotor blade. The far wake of the wind turbine is more homogenous, confirmed by the increased magnitude of the anisotropy factor. By contrast, the channel flow exhibits many anisotropic states of turbulence. In the inner layer of the wall-bounded region, one observes one-component turbulence at the wall; immediately above, the turbulence is dominated by two components, with the outer layer showing fully three-dimensional turbulence, conforming to theory for wall-bounded turbulence. The complexity of flow descriptions resulting from truncated POD bases can be greatly mitigated by severe basis truncations. However, the current work demonstrates that such simplification necessarily exaggerates the anisotropy of the modeled flow and, in extreme cases, can lead to the loss of three-dimensionality. Application of simple corrections to the low-order descriptions of the Reynolds stress tensor significantly reduces the residual root-mean-square error. Similar error reduction is seen in the anisotropy tensor invariants. Corrections of this form reintroduce three-dimensionality to severe truncations of POD bases. A threshold for truncating the POD basis based on the equivalent anisotropy factor for each measurement set required many more modes than a threshold based on energy. The mode requirement to reach the anisotropy threshold after correction is reduced by a full order of magnitude for all example data sets, ensuring that economical low-dimensional models account for the isotropic quality of the turbulence field.

I. INTRODUCTION

Proper orthogonal decomposition (POD) is a well-known tool used extensively in the analysis of turbulent flows for the purposes of identifying and organizing structures according to their energy. Through a series of projections of the ensemble of input signals onto a vectorial subspace, POD produces the optimal modal basis (in a least-squares sense) to describe the kernel of the decomposition. In terms of turbulent flows, the kernel is commonly composed of the correlation tensor [1,2], and the eigenvalues describe the energy associated with each mode. As such, POD is capable of representing the dominant turbulent flow features (in terms of energy) with a small portion of the full mode basis. Since its introduction to the field of turbulence by Lumley [3], POD has evolved considerably, most notably by Sirovich [4], who along with advancements in particle image velocimetry (PIV) technology, pioneered the method of snapshots. This widely used variant

of POD capitalizes on spatial organization of data resulting from experimental techniques such as PIV and numerical simulations.

Often, the basis of POD modes is truncated to exclude contributions to the flow from low-energy modes. Such descriptions of the flow are typically made with small numbers of modes relative to the complete basis [5–7]. Because POD organizes the resultant modes in terms of their contribution to the turbulence kinetic energy, large-scale features of the flow are often well represented with very few modes. While they account for the majority of turbulence kinetic energy, the largest modes selected by the POD also represent the geometry-dependent, anisotropic structures of a turbulent flow. Contrarily, the modes toward the end of the spectrum of the POD basis are taken to be the smallest in terms of energy and the most isotropic contribution to the turbulence. Often when truncating the POD basis for the purpose of a simplified flow description, a threshold is established accounting for a prescribed portion of the turbulence kinetic energy according to the eigenvalues associated with each POD mode.

Anisotropy tensor invariant analysis is often employed to characterize turbulence and to underpin assumptions used in theoretical development [8,9]. The second and third mathematical invariants of the normalized Reynolds stress anisotropy tensor together describe the possible states of realizable turbulence, represented with the anisotropy invariant map, referred to as an AIM, or Lumley's triangle [10]. Theoretical development of the anisotropic state of turbulence has further been employed in predictive models of turbulence often seen in the form of boundary conditions, as for wall-bounded turbulence. Anisotropy tensor invariants are integral to the Rotta [11] model, which describes the tendency of turbulence to return to an isotropic state at a rate linearly proportional to the degree of anisotropy in a turbulent flow. The Rotta model forms the basis of many second-order closure schemes such as the explicit algebraic models of turbulence as presented in Menter *et al.* [12] and Rodi and Bergeles [13].

Anisotropic turbulence evolving in a flat-plate boundary layer was detailed by Mestayer [14], confirming that local isotropy exists in the dissipative range of scales, typically smaller than 20 times the Kolmogorov microscale. Local isotropy at small scales is generally accepted at sufficiently high Reynolds number, provided that an inertial subrange separates the energetic scales from the dissipative ones. It was further shown by Smalley *et al.* [15] and Leonardi *et al.* [16] that surface characteristics of the wall influence the balance of turbulent stresses and subsequently the invariants of the anisotropy tensor. Normal stresses tend toward isotropy in boundary layers evolving over rough surfaces more than over smooth walls. Smyth and Moum [17] found that anisotropy in large-scale turbulence generates Reynolds stresses that contribute to the extraction of energy from the atmospheric boundary layer. Computational work detailing the anisotropy of turbulence in the wakes of wind turbines has been undertaken by Gómez-Elvira *et al.* [18] and Jiménez *et al.* [19]. Both studies employ a second-order closure scheme with explicit algebraic models for the components of the turbulent stress tensor. Recent experimental work by Hamilton and Cal [20] explored the anisotropy in wind turbine arrays wherein the rotational sense of the turbine rotors varied. There, it was found that the flux of mean flow kinetic energy and the production of turbulence correlate with the invariants of the normalized Reynolds stress anisotropy tensor.

Local and small-scale isotropy is expected in the dissipative range of turbulent scales or far from any bounding geometry of the flow, as in the outer boundary layer [11] or far into a wake [18,21,22]. However, large scales, such as those associated with low-rank POD modes, favor the most energetic and the *least* isotropic, turbulence structures. Error propagation through the POD mode basis has been explored to some degree as far as implications to reduced-order models (see, e.g., Refs. [23–26]). The propagation of error through data-driven POD representations of turbulence remains a subject requiring development. Absent from the literature is the dependence of the anisotropy tensor invariants on the point of basis truncation. Reduced-order models aim to capture and reproduce important turbulent flow features. Physical insights gained from such models should include an informed discussion of the anisotropic state of the simulated turbulence as compared to turbulence seen in real flows.

The following work develops the relationship between low-dimensional representations of turbulence via POD and the resulting turbulence field in terms of the Reynolds stress tensor and the

anisotropy tensor invariants. Error propagation of the Reynolds stresses and turbulence kinetic energy are compared to the invariants of the normalized anisotropy tensor as functions of the truncation point of POD models. Low-order descriptions are found to exaggerate the anisotropy of a given flow; modes excluded from the truncated POD basis supply highly isotropic turbulence. Severe basis truncations are unable to reproduce three-dimensional turbulence on their own. With the aid of correction terms, more accurate and realistic turbulence is produced including three-dimensionality, and flow description errors are significantly reduced.

II. THEORY

A. Anisotropy of the turbulent stress tensor

In the following development lower case letters imply mean-centered fluctuations, and an overbar indicates that the ensemble average of the product of fluctuating quantities has been taken. The discussion of turbulence anisotropy necessarily begins with the Reynolds stress tensor, of which the diagonal terms are normal stresses and off-diagonal terms representative of shear stresses in the flow. According to convention, the Reynolds stress tensor is written as

$$\overline{u_i u_j} = \begin{bmatrix} \overline{u^2} & \overline{uv} & \overline{uw} \\ \overline{vu} & \overline{v^2} & \overline{vw} \\ \overline{wu} & \overline{wv} & \overline{w^2} \end{bmatrix}, \tag{1}$$

where u, v, and w distinguish components of fluctuating velocity in the streamwise, wall-normal, and spanwise directions, respectively. The Reynolds stress tensor is symmetric, arising from the Reynolds averaging process. The turbulence kinetic energy, TKE or k, is defined as half of the trace of $\overline{u_i u_j}$:

$$k = \tfrac{1}{2}(\overline{u^2} + \overline{v^2} + \overline{w^2}). \tag{2}$$

The turbulence kinetic energy in Eq. (2) reflects the mean kinetic energy in the fluctuating velocity field and acts as a scale for the components of the Reynolds stress tensor.

The particular balance of terms in the Reynolds stress tensor is important when considering turbulent transport phenomena. In an ensemble sense, isotropic turbulence does not contribute to a net flux in any particular direction, as what is instantaneously transported in one direction would be balanced by an equal and opposite transport at a later time [27]. To quantify deviation from an isotropic stress field, it is useful to define the Reynolds stress anisotropy tensor b_{ij}, normalized with the turbulence kinetic energy, as in the development by Rotta [11],

$$b_{ij} = \frac{\overline{u_i u_j}}{\overline{u_k u_k}} - \frac{1}{3}\delta_{ij}, \tag{3a}$$

$$= \begin{bmatrix} \frac{\overline{u^2}}{\overline{u^2}+\overline{v^2}+\overline{w^2}} - \frac{1}{3} & \frac{\overline{uv}}{\overline{u^2}+\overline{v^2}+\overline{w^2}} & \frac{\overline{uw}}{\overline{u^2}+\overline{v^2}+\overline{w^2}} \\ \frac{\overline{uv}}{\overline{u^2}+\overline{v^2}+\overline{w^2}} & \frac{\overline{v^2}}{\overline{u^2}+\overline{v^2}+\overline{w^2}} - \frac{1}{3} & \frac{\overline{vw}}{\overline{u^2}+\overline{v^2}+\overline{w^2}} \\ \frac{\overline{uw}}{\overline{u^2}+\overline{v^2}+\overline{w^2}} & \frac{\overline{vw}}{\overline{u^2}+\overline{v^2}+\overline{w^2}} & \frac{\overline{w^2}}{\overline{u^2}+\overline{v^2}+\overline{w^2}} - \frac{1}{3} \end{bmatrix}, \tag{3b}$$

where δ_{ij} is the Kronecker delta.

The first invariant of the normalized anisotropy tensor, the trace of b_{ij}, is identically zero as a consequence of its normalization. The traces of b_{ij}^2 and b_{ij}^3 are related to the second and third invariants (η and ξ) of the anisotropy tensor as

$$6\eta^2 = b_{ii}^2 = b_{ij}b_{ji}, \tag{4}$$

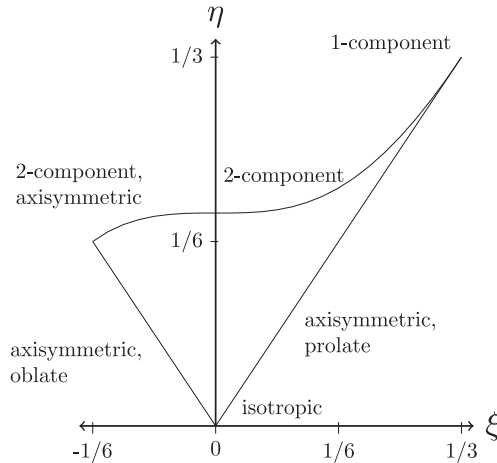$$6\xi^3 = b_{ii}^3 = b_{ij}b_{jk}b_{ki}. \tag{5}$$

FIG. 1. Lumley's triangle showing limits of realizable turbulence according to the anisotropy tensor invariants η and ξ.

Invariants of the normalized Reynolds stress anisotropy tensor express the local degree of three-dimensionality in turbulence (η) and characteristic shape associated with the particular balance of stresses (ξ). The invariants are combined into a single parameter F that scales the degree of anisotropy from zero to one, ranging to one- or two-component turbulence to fully three-dimensional and isotropic turbulence, respectively [15,28]. With the present definitions of invariants, the anisotropy factor is defined as

$$F = 1 - 27\eta^2 + 52\xi^3. \tag{6}$$

In the ensuing analysis, the anisotropy factor is often integrated over the domain (denoted below as F_{int}) to provide an effective value of the anisotropy. F_{int} is presented along side the invariants η and ξ and is used to gauge the degree of anisotropy in each measurement domain.

Invariants of b_{ij} are frequently plotted against one another in the anisotropy invariant map (AIM) [10]. Theoretical limits and special forms of turbulence are shown as vertices or edges of the triangle in Fig. 1. These cases are often used in scale analysis of flows and represent theoretical limits of "realizable" turbulence. See Table I for descriptions of each state of turbulence in terms of their respective invariants. The invariants may also be defined with the eigenvalues of the normalized Reynolds stress anisotropy tensor. Such eigenvalues are interpreted as the spheroidal radii of shapes that characterize the turbulence anisotropy and correspond to the limits shown in Lumley's triangle (see, e.g., Ref. [20]). Characteristic shapes for special cases of turbulence are noted in Table I.

Special cases of turbulence outlined in Table I are used in scaling and theoretical development but are not often observed in real turbulence. Perfectly isotropic turbulence occurs when the deviatoric

TABLE I. Limiting cases of turbulence given on Lumley's triangle in terms of anisotropy tensor invariants.

State of turbulence	Invariants	Shape of spheroid
Isotropic	$\xi = \eta = 0$	Sphere
Two-component axisymmetric	$\xi = -\frac{1}{6}, \eta = \frac{1}{6}$	Disk
One-component	$\xi = \eta = \frac{1}{3}$	Line
Axisymmetric (one large eigenvalue)	$\xi = \eta$	Prolate spheroid
Axisymmetric (one small eigenvalue)	$-\xi = \eta$	Oblate spheroid
Two-component	$\eta = (\frac{1}{27} + 2\xi^3)^{1/2}$	Ellipse

of the Reynolds stress tensor (the anisotropy tensor) is null and $\xi = \eta = 0$. Due to the mathematical relationship between the invariants given by equations (4) and (5), $\xi = 0$ occurs *only* when $\eta = 0$, at the perfectly isotropic condition. The upper limit in Lumley's triangle describes two-component turbulence, where $\eta = (1/27 + 2\xi^3)^{1/2}$. This relationship corresponds to the point where $F = 0$ and is reflected in the definition of F from Eq. (6).

Axisymmetric turbulence is commonly observed in round jets, circular disk wakes, swirling jets, etc. The characteristic shapes associated with axisymmetric turbulence are either oblate or prolate spheroids. Oblate spheroids exhibit two eigenvalues that are of equal magnitude and one eigenvalue that is much smaller. This results in a spheroid squeezed in one direction. Prolate spheroids show the opposite effect with one eigenvalue that is of a larger magnitude compared to the other (equal or very similar) eigenvalues, resulting in a spheroid that is stretched in one direction.

One-component turbulence shows the least uniformity between components and the greatest sensitivity to rotation. Two-component turbulence occurs as the small eigenvalue is reduced to zero, and the characteristic shape becomes an ellipse. In two-dimensional axisymmetric turbulence, the characteristic shape is a circle and is invariant to rotation only along the axis defined by its null eigenvalue.

B. Snapshot proper orthogonal decomposition

Snapshot POD presented below follows the development by Sirovich [4]. The decomposition provides an ordered set of modes and associated eigenvalues delineating the energy associated with each mode. The organized basis of modes from POD has been described as projections common to the span of snapshots in a data set [1,4,29]. Hereafter, bold math symbols represent vectorial quantities and symbols in plain text are scalar quantities. The flow field is assumed to be stochastic and to depend on both space and time. Vectorial velocity snapshots are then denoted as $\boldsymbol{u}(\boldsymbol{x}, t^m)$, where $\boldsymbol{x}$ and t^m refer to the spatial coordinates and time at sample m, respectively. The spatial correlation tensor forms the POD kernel and is defined as

$$\boldsymbol{R}(\boldsymbol{x}, \boldsymbol{x}') = \frac{1}{M} \sum_{m=1}^{M} \boldsymbol{u}(\boldsymbol{x}, t^m) \boldsymbol{u}^T(\boldsymbol{x}', t^m), \tag{7}$$

where M signifies the number of snapshots, the prime represents the spatial coordinate of another point in the domain, and the superscript T refers to the transpose of the velocity field. The POD equation is a Fredholm integral equation of the second kind over the spatial domain Ω:

$$\int_{\Omega} \boldsymbol{R}(\boldsymbol{x}, \boldsymbol{x}') \boldsymbol{\Phi}(\boldsymbol{x}') \, d\boldsymbol{x}' = \lambda \boldsymbol{\Phi}(\boldsymbol{x}). \tag{8}$$

Equation (7) is substituted into Eq. (8) and discretized such that the POD integral equation may be solved numerically. The discretized integral equation becomes an eigenvalue problem in following form:

$$\boldsymbol{C}\boldsymbol{A} = \lambda \boldsymbol{A}, \tag{9}$$

where $\boldsymbol{A}$ is the basis of eigenvectors corresponding to the snapshot basis and $\boldsymbol{C}$ approximates the correlation tensor from Eq. (7). Eigenvalues of the POD equation λ delineate the integrated turbulence kinetic energy associated with each eigenvector and POD mode, which are computed by projecting the snapshot basis into the eigenvector space and normalizing with their respective L^2 norms forming an orthonormal basis:

$$\boldsymbol{\Phi}^{(n)}(\boldsymbol{x}) = \frac{\sum_{n=1}^{N} A^n(t^m) \boldsymbol{u}(\boldsymbol{x}, t^m)}{\left\| \sum_{n=1}^{N} A^n(t^m) \boldsymbol{u}(\boldsymbol{x}, t^m) \right\|}, \quad n = 1, \ldots, N. \tag{10}$$
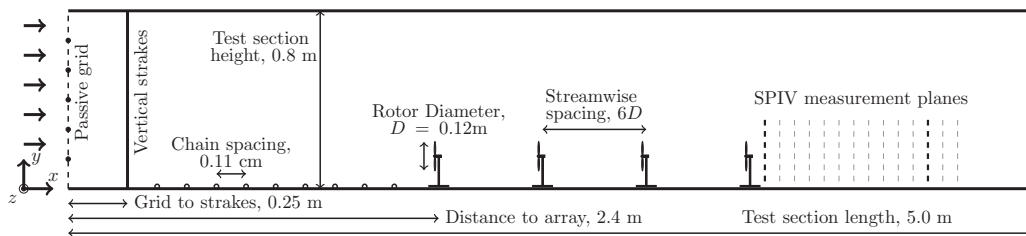
FIG. 2. Schematic of experimental arrangement of wind turbine array. Measurement planes are shown as black dashed lines and occur at $x/D \in [0.5, 6]$ following the fourth row turbine in the center of the tunnel.

The velocity snapshots may be represented as the superposition of the POD modes and respective amplitudes, typically referred to as POD coefficients:

$$\boldsymbol{u}(\boldsymbol{x}, t^m) = \sum_{n=1}^{N} a_n(t^m) \boldsymbol{\Phi}^{(n)}(\boldsymbol{x}). \tag{11}$$

POD mode coefficients a_n are obtained by back-projecting the set of velocity fields onto the basis of POD modes and integrating over the domain:

$$a_n(t^m) = \int_{\Omega} \boldsymbol{u}(\boldsymbol{x}, t^m) \boldsymbol{\Phi}^{(n)}(\boldsymbol{x}) \, d\boldsymbol{x}. \tag{12}$$

Reconstruction with a limited set of POD modes results in a filtered representation of the turbulent flow field. The truncation point of the POD mode basis is often determined by setting an arbitrary threshold of the energy described by the eigenvalues ($\lambda^{(n)}$).

III. EXAMPLE DATA

The following POD evaluation through anisotropy invariant analysis is demonstrated using multiple data sets in order to provide generality. Data samples are of similar geometry and orientation with respect to the mean flow field; all data are two-dimensional, three component snapshots where the mean flow is normal to the plane. The nature of the sampled flow differs in geometry and focus; the first set of data is experimentally acquired via stereo-PIV (particle image velocimetry) in wind tunnel experiments at Portland State University. As the data are used exclusively to illustrate the accuracy of the representations of physical processes, only a summary of the experiment is provided. Further details of the data collection and experimental techniques may be found in Hamilton *et al.* [30,31]. The second set of data comes from DNS (direct numerical simulation) of a fully developed channel flow hosted at Johns Hopkins University (JHU). The reader is referred to the documentation provided by JHU and summarized in Graham *et al.* [32] (see also Refs. [33,34]). Through investigation of several sets of data, focus is placed on interpretation the physics presented through POD and anisotropy invariant analyses, rather than a detailed exploration of each turbulent flow.

A. Wind turbine wake: Experimental data

For the purposes of detailing the streamwise evolution of the turbulent wake behind a wind turbine in a large array, successive SPIV planes were interrogated parallel to the swept area of the rotor of a selected model turbine. The wind turbine array consisted of four rows and three columns of models arranged in a rectangular Cartesian grid; rows are spaced six rotor diameters ($6D$) apart in the streamwise direction, columns are spaced three rotor diameters ($3D$) apart in the spanwise direction. Figure 2 shows the arrangement of wind turbine models in the wind tunnel in addition to the measurement planes.

Although many planes were sampled in the experiment, only two of them will be discussed in the following, selected as representations of different regions of the wake. Figure 2 shows the selected
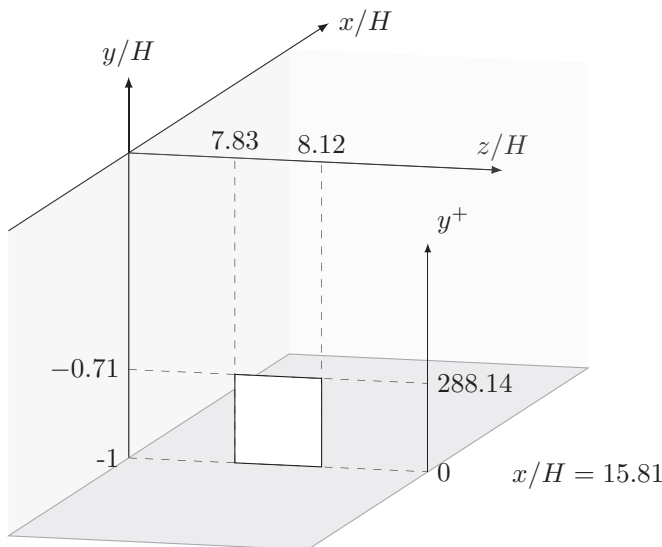
FIG. 3. Schematic of the lower half of the channel flow DNS simulation space. Only a small region of the total channel is shown. Sampling window (white rectangle) was sized to span the inner layers. Location of the window in x/H and z/H was selected randomly.

planes as bold dashed lines in the wake of the fourth row of wind turbines. Sample data correspond to measurements at $x/D = 0.5$, reflecting the near wake where the intermittency is greatest [35], and $x/D = 6$ in the far wake, where the momentum deficit in the wake has largely recovered and the flow is well-mixed [36]. Turbulence statistics at $x/D = 6$ represents the flow that would be seen by successive rows of devices.

B. Turbulent channel flow: DNS data

Direct numerical simulation data of a fully developed channel flow from the Turbulence Database hosted at Johns Hopkins University is compared to the wind turbine wake data. The Reynolds number based on the bulk velocity and full channel height is $\mathrm{Re}_b = U_b 2H/\nu = 4 \times 10^4$, where $U_b = 1$ is the dimensionless bulk velocity integrated over the channel cross section, $H = 1$ is the channel half-height, and $\nu = 5 \times 10^{-5}$ is the nondimensional viscosity. Based on the friction velocity $u_\tau = 5 \times 10^{-2}$ and H, the Reynolds number is $\mathrm{Re}_\tau = u_\tau H/\nu = 1000$. A single spanwise plane representing a small subset of the total channel flow DNS data is discussed in the following analysis, see Fig. 3. The particular location of the plane was fixed for all samples at a randomly selected position along both the x and z coordinates. The near-wall region was of particular interest for the current study as it is well-characterized by anisotropic turbulence. Data span from $-1 \leqslant y/H \leqslant -0.7114$ representing one fourth of the data points across the channel. In viscous units $y^+ = yu_\tau/\nu$, sample data span $0 \leqslant y^+ \leqslant 288$, where the viscous length scale $\delta_\nu = \nu/u_\tau = 1 \times 10^{-3}$. Resolution of the sample data corresponds to that of the full DNS in the spanwise direction $\Delta z/H = 6.13 \times 10^{-3}$, again normalized by the channel half-height. A total of 1180 uncorrelated snapshots were randomly sampled from the channel flow throughout the full simulation time of $t \in [0,26]$.

Spatial limits of the sampled DNS data were selected to focus on the near-wall turbulence. The maximum wall-normal distance of $y/H = -0.7114$ corresponds to half of the logarithmically spaced data points from the wall to the center of the channel. The spanwise limit was set to represent the same total span, resulting in a square measurement window. Data analyzed here cover the viscous sublayer, buffer layer, and the log layer. Turbulence seen in the central region of the channel is expected to exhibit the passage of large, anisotropic structures, although in an ensemble sense,
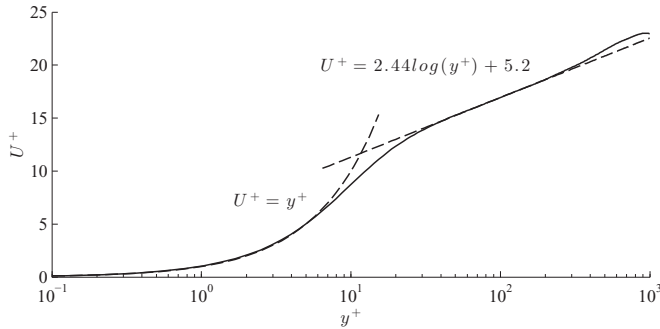
FIG. 4. Half-channel velocity profile. Dashed lines correspond to the viscous sublayer and the log layer.

the turbulence there is more isotropic. The half-channel velocity profile is shown in viscous units ($U^+ = u/u_\tau$ vs y^+) in Fig. 4. As reference, two Reynolds stresses are shown from the DNS of the channel flow in Fig. 5. The stresses shown are the streamwise normal stress and the shear stress combining fluctuations in the streamwise and wall-normal velocities.

IV. RESULTS

Results pertaining to the example data are reviewed in several stages: a brief review of the turbulence statistics followed by the corresponding Reynolds stress anisotropy tensor invariant analysis, and the proper orthogonal decomposition. Analytical methods are then combined and discussed in terms of the anisotropy of the turbulence field as represented through truncated POD bases. Finally, effects of a least-square correction applied low-order descriptions are discussed in terms of error reduction.

A. Turbulence field

The first SPIV plane discussed is located at one half rotor diameter downstream from the model wind turbine ($x/D = 0.5$) and represents the location of greatest intermittency imparted on the flow by the passage of the rotor blades. At this location, evidence of the rotor is quite clear in each component of the Reynolds stress tensor, seen in Fig. 6. An artifact resulting from a reflection is seen in the area about $(z/D, y/D) = (0.35, 0.4)$ in many of the contour plots in Fig. 6.
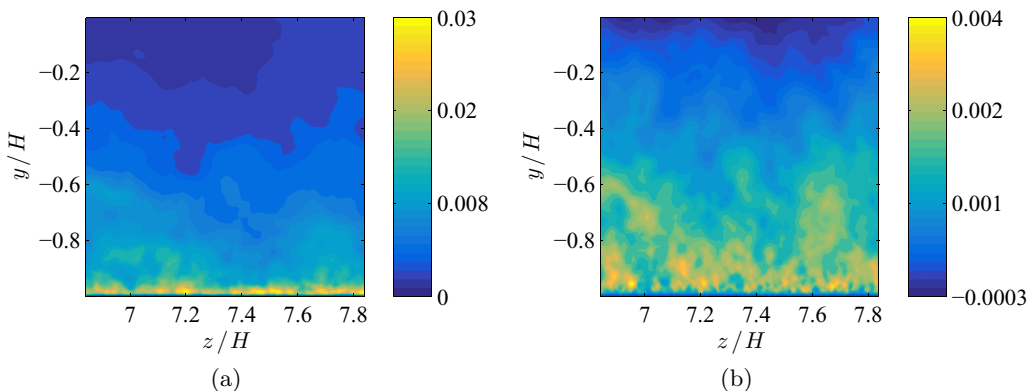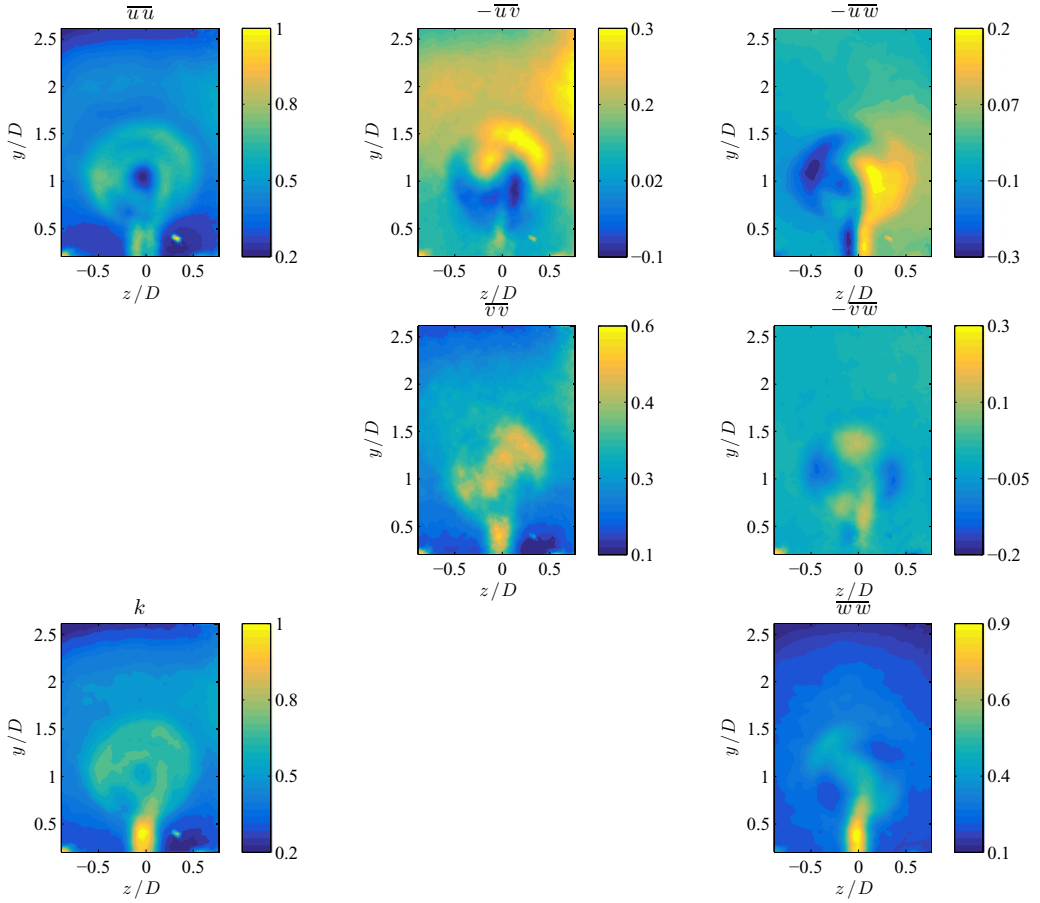

FIG. 5. Turbulent stresses spanning the half-height of the channel flow. (a) Streamwise normal stress $\overline{uu}$. (b) Reynolds shear stress $-\overline{uv}$.

FIG. 6. Reynolds stresses and k from the wake of a wind turbine at $x/D = 0.5$.

The Reynolds normal stresses ($\overline{uu}$, $\overline{vv}$, and $\overline{ww}$) are shown in the diagonal positions of Fig. 6. Together, they account for the energy described by k. All the normal stresses exhibit high magnitudes following the mast of the model turbine. The streamwise normal stress shows peak values tracing the swept area of the roots and tips of the rotor blades. Minimum values of $\overline{uu}$ follow the nacelle of the model turbine. The vertical normal stress $\overline{vv}$ shows an area of high magnitudes combining several effects. Vertical fluctuations in the wake are greatest in intensity issuing from the rotor at top-tip and bottom tip heights, rotated by the bulk flow field. An analogous effect is seen for $\overline{ww}$ where the greatest fluctuations occur at the spanwise extremes of the rotor and are similarly rotated in the wake by the bulk flow.

Asymmetry of the wake arising from the rotating geometry of the wind turbine is evident in the Reynolds shear stresses, especially those including fluctuations of the streamwise velocity. As expected from other wind tunnel studies for wind energy [36–38], positive values of $-\overline{uv}$ occur above hub height in the wake. This component of the Reynolds shear stresses is associated with the vertical flux of mean flow kinetic energy by turbulence and remediation of the wake. Correlations between the streamwise and spanwise fluctuations of velocity are seen in the contour plot of $-\overline{uw}$ and contribute to lateral flux of kinetic energy. Rotation of the turbine rotor influences $-\overline{uv}$ and $-\overline{uw}$ similar to the normal stresses discussed above. The Reynolds shear stress $-\overline{vw}$ is approximately symmetrical about the hub in both the xy and xz planes.
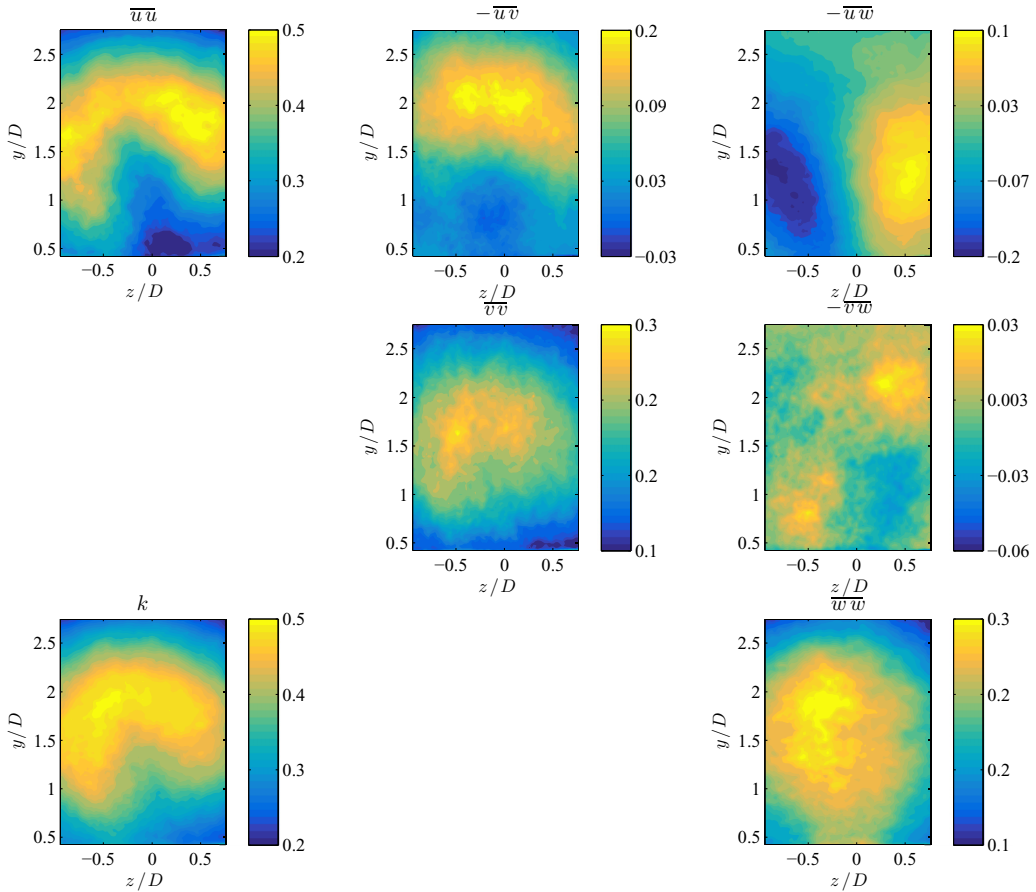
FIG. 7. Reynolds stresses and k from the wake of a wind turbine at $x/D = 6$.

In the bottom left corner of Fig. 6 is a contour plot of the turbulence kinetic energy k. It is unsurprising that the dominant features of k correspond with those of $\overline{uu}$, as it is the largest component of the Reynolds stress tensor for the presented data. The turbulence kinetic energy is included for its theoretical contribution to the present analysis methods; turbulence kinetic energy integrated over the measurement domain is reflected by the POD eigenvalues, and it is used to normalize the Reynolds stress tensor in arriving at the anisotropy tensor.

A measurement plane from the far wake was at $x/D = 6$ as the turbulence exhibits different behavior here than near the model wind turbine, see Fig. 7. At this location the wake deficit is largely recovered and the flow is well-mixed. Each of the turbulent stresses is more uniformly distributed in the measurement plane and has decreased in magnitude from the previous examples. Evidence of rotation is almost completely absent from the normal stresses with the exception of $\overline{uu}$, which continues to demonstrate some asymmetry.

The magnitudes of the shear stresses are greatly reduced compared to their previous values. Those stresses contributing to the flux of kinetic energy ($-\overline{uv}$ and $-\overline{uw}$) demonstrate magnitudes less than 50% of their corresponding near-wake values, indicating that the turbulence is fairly uniform at this point in the wake. The stress $-\overline{vw}$ has reduced in magnitude to approximately 10% of its former level, although it retains the features seen throughout the wake. Although they differ slightly in magnitudes, each of the normal stresses demonstrate that the flow tends toward homogeneity far into the wake. As the shear terms fall off, one may also consider that the normal terms become more representative of the principle stresses. This tendency toward uniformity is characteristic of
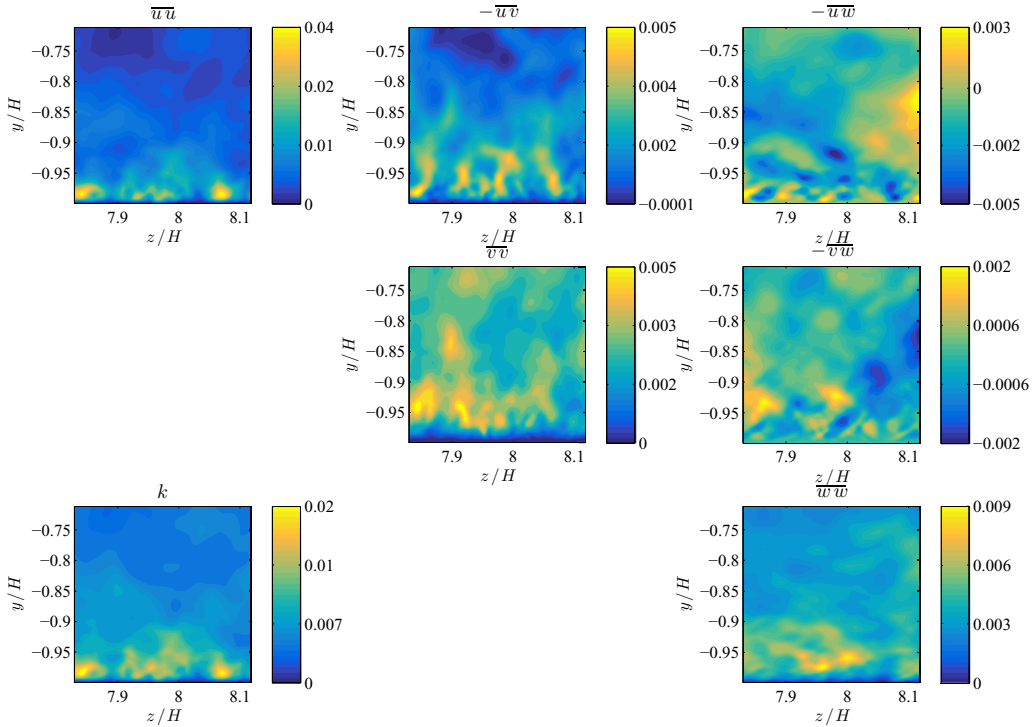
FIG. 8. Reynolds stresses and k from the fully developed channel flow DNS.

well-mixed turbulence and is reflected in the invariants of the normalized Reynolds stress anisotropy tensor.

Data from the DNS of the fully developed channel flow are seen in Fig. 8. A small subset of the total channel flow data are shown following the same presentation as the wind turbine wake; downsampling of the full data accounts for limited statistical convergence. The data included here were intentionally downsampled, both spatially and temporally, for the purposes of low-order description. Regardless of downsampling, the characteristic features of the turbulence close to the wall on one side of the channel are represented in the contours in Fig. 8.

Reynolds stresses presented for the channel flow differ from those of the wind turbine wake; the spatial organization of energy present in each component of the stress tensor reflects the influence of the wall on the flow. Direct numerical simulation undertaken here is the product of extensive technical development such that the resulting turbulence field matches boundary conditions derived theoretically and observed in closely controlled experiments. The inner layer of the wall-bounded region in the simulation yields minimum values of all components of the Reynolds stress tensor. Profiles of the stress field are seen in the associated documentation [32] with greater statistical convergence.

The simulation data include boundary conditions applied at the wall as identically null values of all Reynolds stresses at $y^+ = 0$. Immediately above the wall, stresses and turbulence kinetic energy take on non-null values. The inner layer is evidenced as the region where viscous forces dominate and the resulting turbulence is low in magnitude. Turbulence stresses increase quickly with y^+; the streamwise normal Reynolds stress and k show peak values at $y^+ = 16.5$ ($y/H \approx -0.9835$). Maximum values of $\overline{vv}$ and $\overline{ww}$ occur further away from the wall. Shear terms are lower in magnitude than the normal stresses and take on negative values in the flow. All stresses from the DNS channel flow are nondimensionalized by the channel half-height H, and the friction velocity $u_\tau = 0.0499$. The DNS was performed with nondimensional values, and as a result each component of $\overline{u_i u_j}$ demonstrates values approximately two orders of magnitude lower than in the wake of the wind
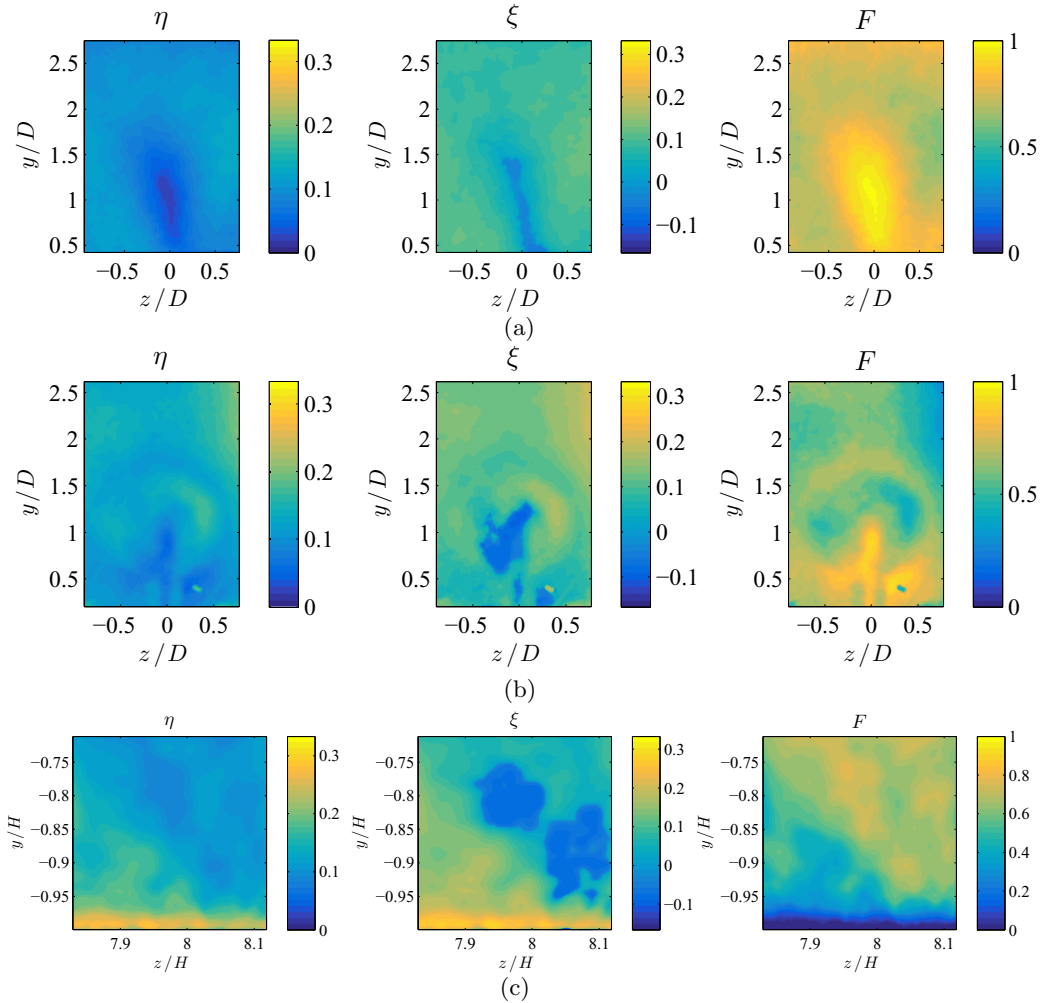
FIG. 9. Contours of the η, ξ, and F, from left. Color range reflects the full theoretical range of each quantity. (a) $x/D = 0.5$, (b) $x/D = 6$, and (c) channel flow DNS.

turbine seen above. In the following review of the anisotropy tensor invariants, it is clear that the anisotropy of a turbulent flow is dependent on the deviation from isotropic turbulence rather than the magnitudes of the Reynolds stress tensor.

B. Reynolds stress anisotropy

The second and third Reynolds stress anisotropy tensor invariants and the anisotropy factor are shown in Fig. 9 for both planes in the wind turbine wake and the channel flow. Agreeing with the Reynolds stresses above, the invariants demonstrate a decrease in spatial organization moving downstream from the model wind turbine. Subfigures correspond to $x/D = 0.5$ in Fig. 9(a), $x/D = 6$ in Fig. 9(b), and the channel flow in Fig. 9(c). Contours of η from the near wake [Fig. 9(a)] indicate that the minimum values occur trailing the nacelle of the turbine close to the device. Increased η indicates a higher degree of anisotropy in the turbulence. Maxima of $\eta \approx 0.22$ occur at the spanwise borders of the wake ($z/D \approx \pm 0.5$) and in the upper corners of the measurement plane. By $x/D = 6$ [Fig. 9(b)], large-scale mixing in the wake increases the uniformity of the turbulence field.
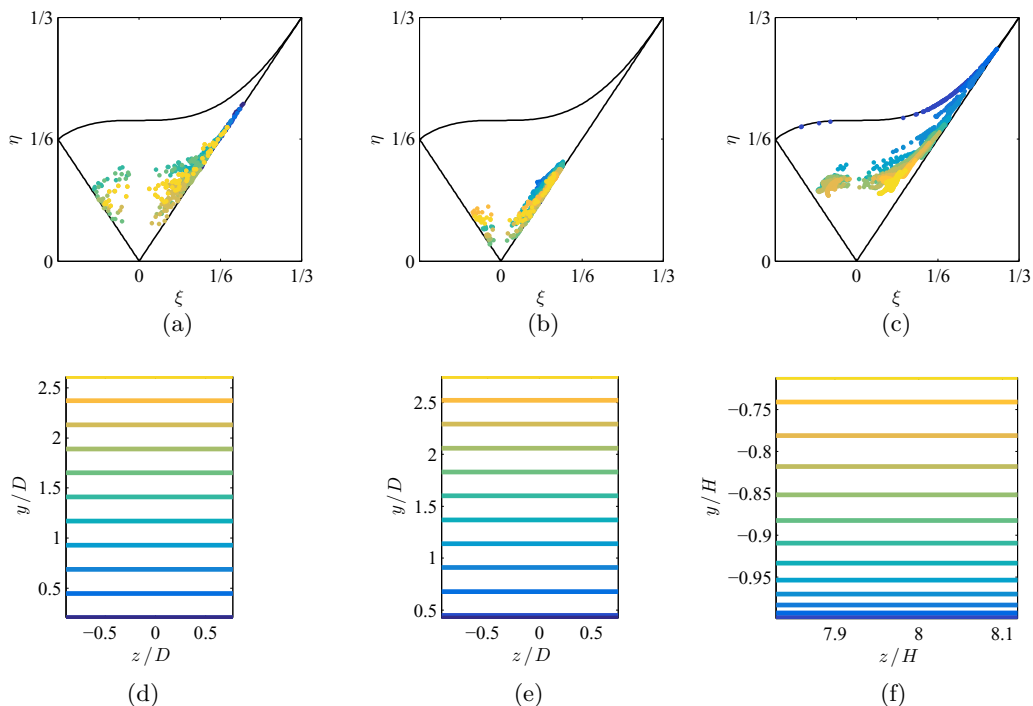
FIG. 10. Anisotropy invariant maps for each measurement set (a)–(c). Points in the invariant space are colored according to their wall-normal location in physical space (d)–(f). (a),(d) $x/D = 0.5$, (b),(e) $x/D = 6$, and (c),(f) channel flow DNS.

Downstream from the wind turbine, turbulence decays and becomes increasingly homogeneous and tends toward isotropy. Accordingly, the second invariant in this case is smaller than the second invariant observed in the near wake.

The third invariant ξ delineates whether the turbulence field is well represented by a single dominant component ($\xi > 0$) or two codominant components ($\xi < 0$). Near the turbine ($x/D = 0.5$), the third invariant shows a region of $\xi < 0$ trailing the mast and the lower part of the rotor area. As with the turbulent stresses, the region of negative ξ is made asymmetric by rotation of the bulk flow. In the far wake ($x/D = 6$), ξ is symmetrically distributed in the wake as effects of rotation are largely absent from the flow at that location. The magnitude of ξ is reduced in the far wake following the transition of the turbulence toward homogeneity. As with η, increasingly isotropic flow requires small magnitudes of ξ.

Figure 9(a) shows that the region of highest F occurs following the nacelle and mast of the model wind turbine and the region of the flow below the rotor. Within the swept area of the rotor, F demonstrates values below 0.5, taken to indicate local anisotropy; immediately outside the swept area of the rotor, $F \approx 0.75$, suggesting that structures shed by the tips of the rotor blades contribute more isotropic turbulence in an ensemble sense. Looking to the far wake in Fig. 9(b), the entire measurement field is more isotropic with peak values on the order of $F \approx 0.95$ following the nacelle. The wake expands as it convects downstream, shown by the regions where $F \approx 0.6$. The channel flow demonstrates the anticipated gradient of F with y/H. Minimum values of F occur at and immediately above the wall; F increases to approximately 0.75 with increasing wall normal coordinate. The data presented here do not include the center of the channel, where F reaches its maximum value.

Lumley's triangles are shown for the SPIV measurement planes in Fig. 10. Points in each Lumley's triangle are colored by their respective wall-normal locations, shown by Figs. 10(d) through 10(f).
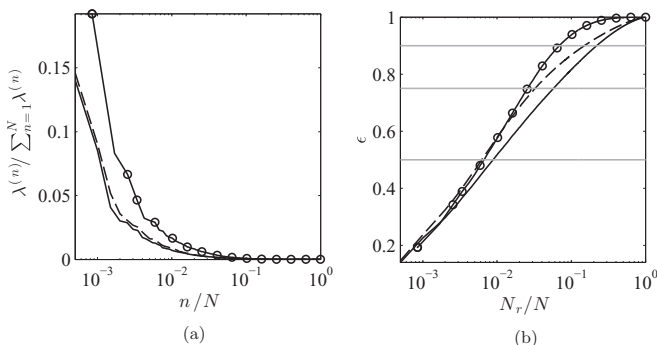
FIG. 11. Eigenvalues from the snapshot POD for the wind turbine wake at $x/D = 0.5$ (solid black lines), $x/D = 6$ (dashed lines), and the channel flow DNS data (line with circles). (a) Normalized eigenvalues from POD of WTA and channel flow, (b) normalized cumulative summation of eigenvalues with thresholds for 50, 75, and 90% integrated turbulence kinetic energy in gray lines.

Dark blue points correspond to the smallest wall-normal coordinate; yellow points correspond to large values of the wall-normal coordinate. For clarity in the anisotropy invariant maps, only the points in Figs. 10(d) through 10(f) are shown. Data for the near wake show that the turbulence occupies a large region of the anisotropy invariant space. Interesting to note is that ξ is always either significantly positive or significantly negative; the center of Lumley's triangle is not occupied by the invariants for $x/D = 0.5$. The wind turbine wake tends toward positive ξ, indicating that the turbulence is dominated by a single large principal stress for much of the wake. Farther downstream, the turbulence is much more isotropic as indicated by the occupation of the lower region of Lumley's triangle at $x/D = 6$, although it never reaches the perfectly isotropic condition, where $\eta = \xi = 0$.

Invariants of the channel flow show different behavior than the wind turbine wake in the near-wall region $y/H < -0.95$, where the magnitudes of both invariants are quite large. This region conforms to boundary conditions imposed on the flow. Turbulent stresses peak in the near-wall region arising from strong shearing of the mean flow. In the viscous sublayer ($y^+ \approx 10$), nearly all turbulence is suppressed. Immediately above the wall, the only non-null Reynolds stress is $\overline{uu}$, there leading to data with identically one-dimensional turbulence ($\eta = \xi = 1/3$). With increasing wall-normal distance, the spanwise normal stress begins to emerge and the turbulence follows the two-component boundary of Lumley's triangle. With increasing y/H, the remaining Reynolds stresses account for some energy, and the invariants shift suddenly to exhibit values corresponding to three-dimensional turbulence. In the outer region of the wall-bounded region ($y^+ \geqslant 50$), the turbulence is less organized in the sense of the anisotropy tensor invariants, meaning that the second invariant spans $0.1 \leqslant \eta \leqslant 0.3$ and the third invariant spans $-0.1 \leqslant \xi \leqslant 0.3$. The turbulence in the center of the channel flow (not shown) is more isotropic than the wall-bounded region. With increasing wall-normal distance, anisotropy invariants follow the trends described by Rotta [11] and Pope [27], where η and ξ tend toward zero with increasing y/H and turbulence becomes more isotropic.

C. Snapshot POD

The two selected measurement planes from the wind turbine wake each have 2000 POD modes corresponding to the 2000 velocity snapshots used to formulate the kernel of the POD integral equation. Each mode is also associated with an eigenvalue that communicates the energy associated with that mode throughout the measurement set. Similarly, the channel flow data have 1180 POD modes issuing from the snapshots sampled from the simulation data. Normalized POD eigenvalues for each data set are seen in Fig. 11(a).

One of the major benefits of POD arises from its ability to sort the resulting modal basis in relation to their relative importance. In this way, features that dominate in terms of their contribution

to the TKE may be selected to represent the full turbulence field with very few modes. Figure 11(b) shows the cumulative summation of the eigenvalues from each data set compared to frequently used thresholds. The point of truncation of a POD mode basis is frequently arbitrary, often taking a threshold of a given portion of the total energy expressed by the POD eigenvalues. Thresholds of these sort are seen in Fig. 11(b) as gray horizontal lines. Reconstructing the Reynolds stress tensor with a truncated set of POD modes typically describes the important features of the turbulence but necessarily excludes energy from the description. The 50% threshold of integrated TKE requires very few modes (8, 13, and 18 modes for the channel flow, wake at $x/D = 6$, and wake at $x/D = 0.5$, respectively) but omits energy from the majority of the modal basis. Intermediate and high modes are taken to describe small scales of turbulence that are relatively isotropic and contribute little energy to the turbulence field. Gray lines in Fig. 11(b) correspond to 50%, 75%, and 90% thresholds of energy expressed by the cumulative summation of POD eigenvalues. Shorthand notation for the cumulative summation of turbulence kinetic energy expressed by a truncated mode basis is introduced as

$$\epsilon = \int_\Omega \mathring{k}\, d\Omega \Big/ \int_\Omega k\, d\Omega = \sum_{n=1}^{N_r} \lambda^{(n)} \Big/ \sum_{n=1}^{N} \lambda^{(n)}, \qquad (13)$$

where the point of truncation is designated by N_r. In Eq. (13), quantities designated with an over-ring (e.g., $\mathring{k}$) represent the truncated turbulence described with the low-rank POD modes.

The flows are easily distinguished by the trends shown in Fig. 11(b). POD eigenvalues from wake data indicate that many more modes are required to recover the full range of dynamics in the flow. Trends for $x/D = 0.5$ and $x/D = 6$ in the solid and dashed lines are flatter than for the channel flow, indicating that there is a broader range of energetic structures in the wake. In contrast, the channel flow data accumulate energy with few modes. Nearly all of the energy is present in the first 100 modes, and the remaining basis describes very little in terms of turbulence kinetic energy. This is due in part to limiting the range of the sampled data to exclude the outer portion of the domain. In wall-bounded flows, the range of length scales observed is a function of wall-normal distance. Applying POD to the channel half-height yields a greater range of POD modes describing energetic structures in the flow. Energy accumulates across the channel half-height faster than in the wake data, seen as a flat region of the eigenvalue spectrum for $N_r/N \geqslant 10^{-1}$.

Figure 11(a) shows that energy associated with each POD mode is normalized by the turbulence kinetic energy integrated over each measurement domain. Each normalized POD eigenvalue describes the relative importance of its respective POD mode to the turbulence field. The distribution of energy in the normalized eigenvalues for the wake measurements (solid and dashed lines) are nearly identical to one another, due to the similarity in POD modes downstream of the turbine. Hamilton *et al.* [31] demonstrated that POD modes are subject to streamwise evolution throughout the wake. Eigenvalues for the channel flow (indicated with circles) fall off more quickly than for the wake. The concentration of energy in few eigenvalues suggests that energy is contained in a few coherent structures that exist in the wall-bounded region of the channel flow.

In the low-order descriptions, the POD basis is separated into isotropic and anisotropic portions analogous to decomposing the turbulence field according to Eq. (3). The isotropic portion of the field is assumed to be accounted for by the small scales, represented by intermediate and high-rank POD modes. The anisotropic contribution to the total turbulence field is represented by the lowest ranking POD modes representing the most energetic structures. The POD eigenvalues delineate the turbulence kinetic energy expressed by the Reynolds stress tensor integrated over the domain, equal to the sum of the isotropic and anisotropic turbulence:

$$\sum_{n=1}^{N} \lambda^{(n)} = \int_\Omega \mathring{k}\, d\Omega + \int_\Omega \hat{k}\, d\Omega. \qquad (14)$$

In the current interpretation of the POD modes, anisotropic contributions to the turbulence field are composed with the lowest ranking POD modes, and the complementary isotropic contributions are designated with the caret (e.g., $\hat{k}$) composed of the remaining POD modes. The majority of turbulence
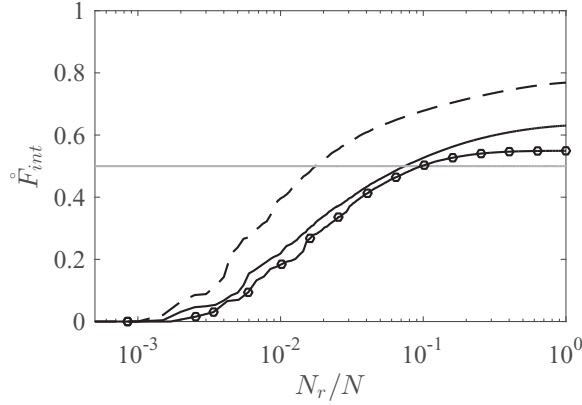
FIG. 12. Equivalent anisotropy factor the wind turbine wake at $x/D = 0.5$ (solid black lines), $x/D = 6$ (dashed lines), and the channel flow DNS data (circles).

structures are considered to be part of the isotropic turbulence field, including contributions from intermediate and high-rank POD modes.

The Reynolds stress tensor is represented as the superposition of modes up to N_r, according to

$$\overline{\overset{\circ}{u_i u_j}} = \sum_{n=1}^{N_r} \lambda^{(n)} \phi_i^{(n)} \phi_j^{(n)}. \tag{15}$$

With the low-order description of the Reynolds stress tensor calculated according to Eq. (15), the anisotropic turbulence kinetic energy is written $\overset{\circ}{k} = \frac{1}{2}(\overline{\overset{\circ}{uu}} + \overline{\overset{\circ}{vv}} + \overline{\overset{\circ}{ww}})$. In the same sense, the isotropic contributions to the turbulence field may be represented with the range of modes from the point of truncation N_r to the end of the basis:

$$\overline{\overset{\wedge}{u_i u_j}} = \sum_{n=N_r+1}^{N} \lambda^{(n)} \phi_i^{(n)} \phi_j^{(n)}. \tag{16}$$

Common practice in low-order descriptions via POD is to establish the truncation point of the modal basis at the point where 50% of the total turbulence kinetic energy is included according to the cumulative summation of $\lambda^{(n)}$ [as seen in Fig. 11(b)]. A division at this point imposes the balance $\int \overset{\circ}{k} d\Omega = \int \hat{k} d\Omega$. Truncating at a desired threshold of energy accounts for much of the dynamic information of the turbulence field with an economy of modes; in fact, POD is defined to do exactly this.

However, an energy threshold offers no guarantee of a quality reconstruction in terms of turbulence isotropy. To this end, the equivalent anisotropy factor F_{int} is computed for each case and shown in Fig. 12 as a function of the number of POD modes used to represent the turbulence field. Theoretically, $\overset{\circ}{F}_{\text{int}}$ ranges from zero for anisotropic (one- or two-dimensional) turbulence to one for isotropic turbulence. In the data shown, $\overset{\circ}{F}_{\text{int}}$ converges to F_{int} with increasing N_r but never reaches unity as the example data exhibit anisotropy throughout the fields. The horizontal gray line included in the figure illustrates a threshold where $F_{\text{int}} = 0.5$, an even division of the range of the anisotropy factor, taken here to separate anisotropic and isotropic turbulence. The three cases demonstrate values of the equivalent anisotropy factor of 0.63, 0.77, and 0.55 for the wind turbine wake at $x/D = 0.5$, $x/D = 6$, and the channel flow, respectively. The equivalent anisotropy factor is an integrated average value over the measurement domain, thus smaller values of F_{int} indicate local contributions of anisotropic turbulence. The number of modes required to reach the $F_{\text{int}} = 0.5$ threshold in each case depends on the number of modes that account for anisotropic features in the

TABLE II. Comparison of energy and anisotropy thresholds for the wind turbine wake and channel flow. The relative portion of energy accounted for by the truncated basis up to N_r is designated as ϵ.

Case	$\epsilon \geqslant 0.5$		$\mathring{F}_{int} \geqslant 0.5$	
$x/D = 0.5$	$N_r = 18$,	$\mathring{F}_{int} = 0.21$	$N_r = 149$,	$\epsilon = 0.78$
$x/D = 6$	$N_r = 13$,	$\mathring{F}_{int} = 0.29$	$N_r = 36$,	$\epsilon = 0.67$
Channel flow	$N_r = 8$,	$\mathring{F}_{int} = 0.13$	$N_r = 115$,	$\epsilon = 0.94$

flow. In the current cases, the $F_{int} = 0.5$ threshold is reached when including $N_r = 149$, 36, and 115 modes for the wind turbine wake at $x/D = 0.5$, $x/D = 6$, and the channel flow, respectively. The number of modes required to reach the anisotropy threshold is much larger than that required to reach the 50% energy threshold in all cases. Table II lists the cases and thresholds including the complementary values in question (in terms of ϵ or $\mathring{F}_{int}$).

Figures 13–15 show reconstructions of components of the Reynolds stress tensor including fluctuations of the streamwise velocity. Each figure compares low-order descriptions of the stresses based on the thresholds on ϵ or $\mathring{F}_{int}$, delineated in Table II. In the contours of Fig. 13(a), one observes that many of the distinctive features seen in the full stress field at $x/D = 0.5$ are represented by $\overline{u_i^{\circ} u_j}$ using the 50% energy threshold, although the magnitude of each stress is reduced in the low-order description. The streamwise normal stress $\overline{u u}$ exhibits azimuthal streaks resulting from passage

FIG. 13. Low-order descriptions of the turbulence field at $x/D = 0.5$ using the kinetic energy threshold (a) using $N_r = 18$ modes and accounting for $\mathring{F}_{int} = 0.21$ and $\epsilon = 0.5$ and the anisotropy factor threshold (b) using $N_r = 149$ modes and accounting for $\mathring{F}_{int} = 0.5$ and $\epsilon = 0.78$.
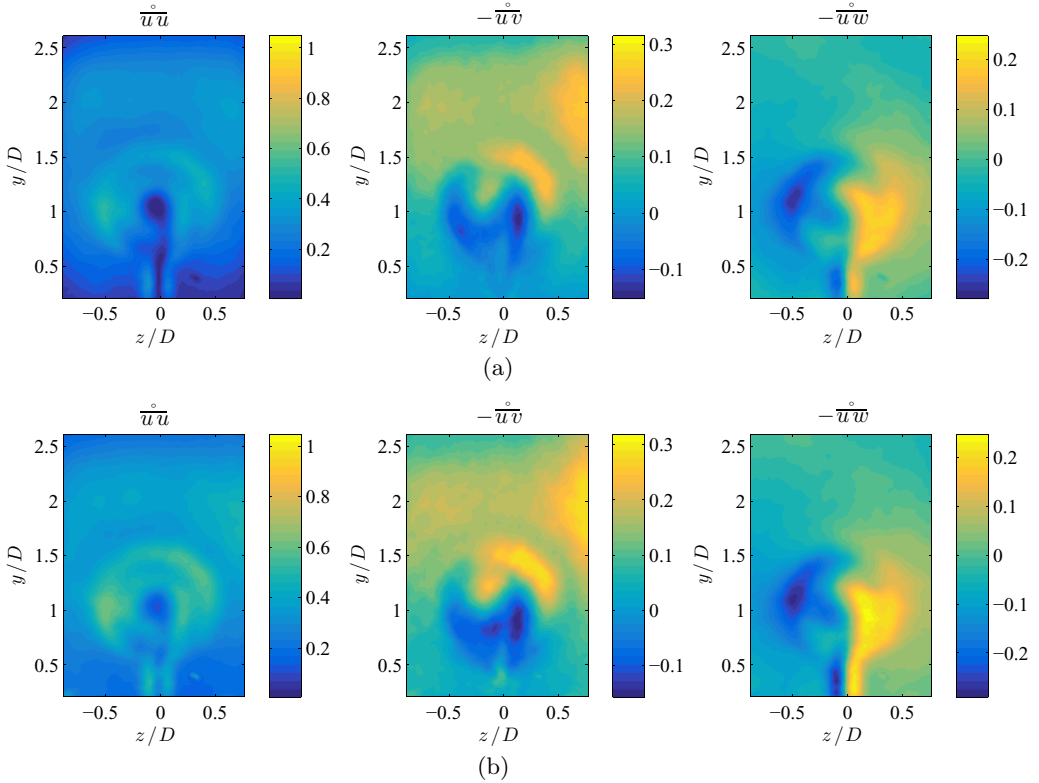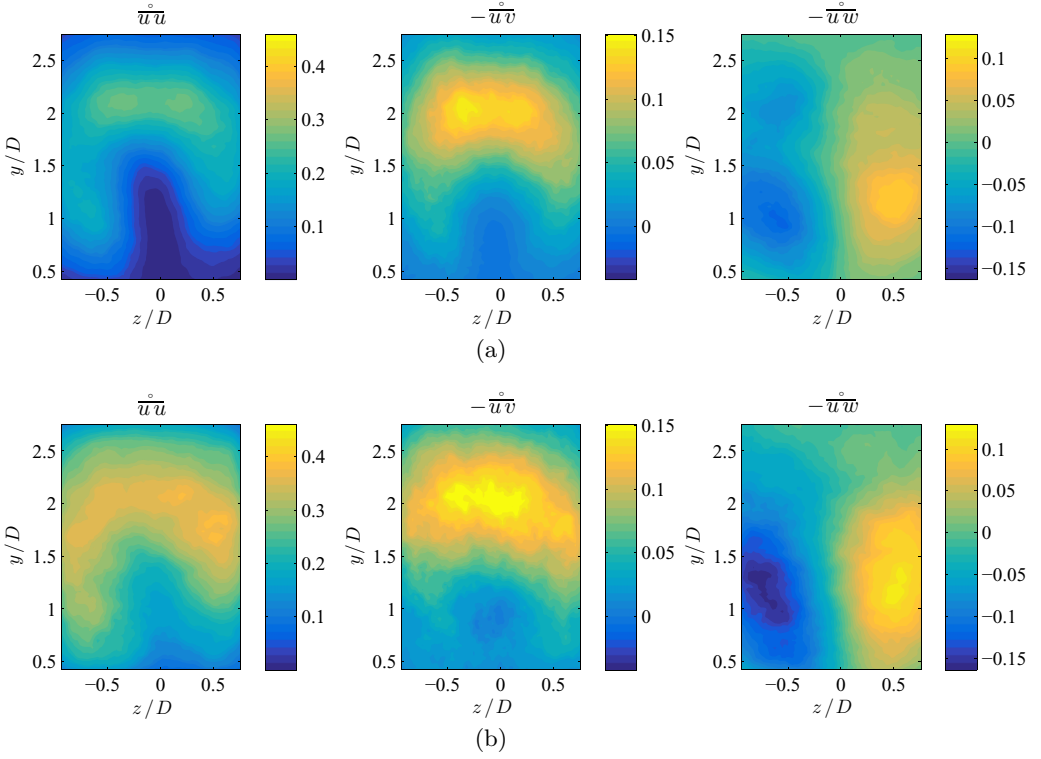
FIG. 14. Low-order descriptions of the turbulence field at $x/D = 6$ using the kinetic energy threshold (a) using $N_r = 13$ modes and accounting for $\mathring{F}_{\text{int}} = 0.29$ and $\epsilon = 0.5$ and the anisotropy factor threshold (b) using $N_r = 36$ modes and accounting for $\mathring{F}_{\text{int}} = 0.5$ and $\epsilon = 0.67$.

of the rotor blades seen in the full statistical values. However, the isotropic portion $\overline{\hat{u}\hat{u}}$ shows no evidence of rotation in the flow. Instead, the isotropic part is nearly uniform in the swept area of the rotor. Similar behavior is seen in the shear stresses in Fig. 13(a). Both $\overline{\mathring{u}\mathring{v}}$ and $\overline{\mathring{u}\mathring{w}}$ show characteristic regions of positive and negative magnitudes and the effects of bulk rotation discussed above. While the most energetically significant dynamics are accounted for in the 50% energy threshold, the equivalent anisotropy factor using only 18 modes is $\mathring{F}_{\text{int}} = 0.21$, which indicates that the anisotropy of low-order description of the turbulence is greatly exaggerated as compared to the original field. Reconstructing the Reynolds stress tensor up to the anisotropy threshold [Fig. 13(b), 149 modes for $x/D = 0.5$] brings the equivalent anisotropy factor up to $\mathring{F}_{\text{int}} = 0.5$, and naturally accounts for more kinetic energy in the modal basis. Interestingly, the contours in Figs. 13(a) and 13(b) are qualitatively similar, the key difference being that using more modes in the description of turbulence increases the magnitude of each stress. This indicates that while many modes are needed to reach the $\mathring{F}_{\text{int}} = 0.5$ threshold, energy introduced in the intermediate range is relatively homogeneously distributed in the field.

A greater difference between the two thresholds is observed for the far wake of the wind turbine. Again, a low-order description recovers the dominant flow features in the field, but the difference in magnitudes is more significant than in the near wake. At $x/D = 6$, the salient features of the stresses are all present in the first 13 modes, seen in Fig. 14(a), but the magnitudes of the Reynolds stresses are as small as 30% of their full statistical values. Comparing $\overline{\mathring{u}_i\mathring{u}_j}$ to $\overline{u_i u_j}$ from Fig. 7, the behavior is accounted for by the anisotropic contribution of 36 modes. Magnitudes of the contours in Fig. 14(b) are approximately 80% of the original statistical values, much closer to the full field.
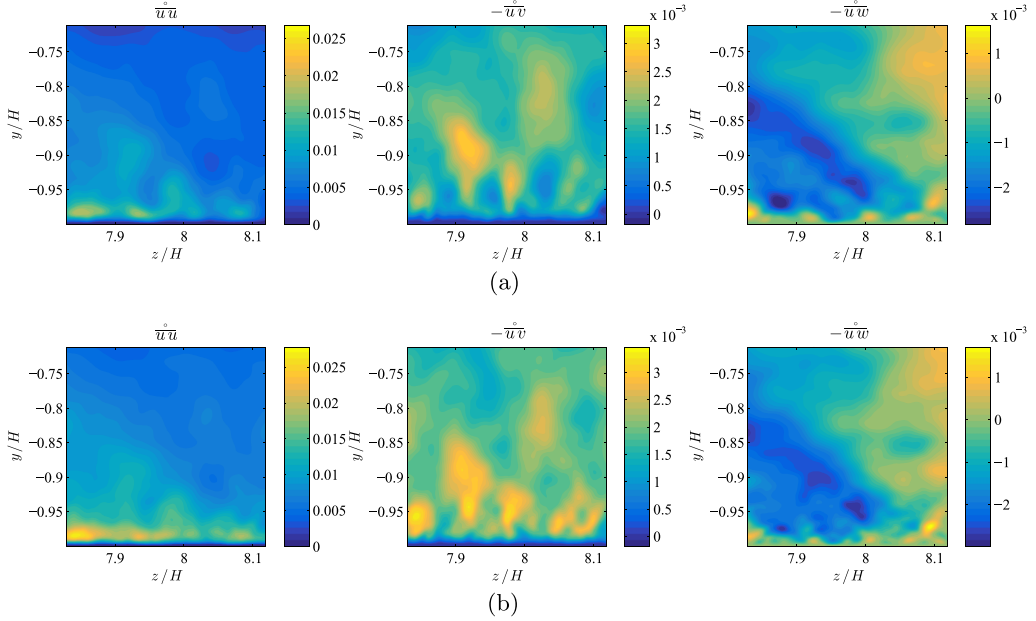
FIG. 15. Low-order descriptions of the turbulence field in the channel flow using the kinetic energy threshold (a) using $N_r = 8$ modes and accounting for $\mathring{F}_{int} = 0.13$ and $\epsilon = 0.5$ and the anisotropy factor threshold (b) using $N_r = 115$ modes and accounting for $\mathring{F}_{int} = 0.5$ and $\epsilon = 0.94$.

Even more than in the near wake, the isotropic contributions are uniform and small for $x/D = 6$. The far wake of the wind turbine exhibits the most isotropic turbulence of the selected data, with a full-order equivalent anisotropy factor of 0.77. Figure 12 confirms that F_{int} is larger for the far wake and that the threshold is reached much more quickly than for the other cases, indicating that a greater range of POD modes contribute isotropic turbulence structures.

Low-order descriptions of the channel flow turbulence are shown in Fig. 15. In the turbulence accounted for by the modes below the 50% energy threshold ($N_r = 8$), magnitudes of the Reynolds stresses in Fig. 15(a) are already quite similar to those shown in the original statistics, although the reconstructed features differ. In the channel flow, the energetic portion of the modal basis is incapable of capturing all of the near-wall behavior. Like the wind turbine wake in Figs. 13 and 14, the shear stresses in the channel flow are nearly identical to the description using the full statistics, although they reconstruct at different rates. The streamwise-spanwise stress $\overline{u\mathring{w}}$ slightly overestimates the shear close to the wall. The $\mathring{F}_{int} = 0.5$ threshold uses many more modes [Fig. 15(b), $N_r = 115$] than the energy threshold for the channel flow. This difference indicates that many intermediate modes are considered anisotropic but contribute little in the way of energy. As anticipated, including more modes results in estimates of the Reynolds stresses with greater detail and magnitudes that are more similar to their respective statistical values.

Gauging the quality of POD reconstructions by comparing their invariants as in Eqs. (4) and (5) yields parallel insights to the customary energy-based analysis. The resulting invariants reveal a great deal about the character of the flow not immediately visible in contours of the stresses. Figure 16 offers a comparison between the AIMs of the invariants of b_{ij}, $\mathring{b}_{ij}$, and $\hat{b}_{ij}$ based on the anisotropy threshold of $\mathring{F}_{int} = 0.5$, from left to right, respectively. The center column of Fig. 16 plots $\mathring{\eta}$ and $\mathring{\xi}$ for the three data cases. All measurement points exhibit invariants greater than in the original data, with the exception of data describing one- or two-component turbulence (these points already show the greatest magnitudes of η allowed for realizable turbulence), confirming that the lowest ranking POD modes correspond to the least isotropic contributions to the turbulence field. Further,
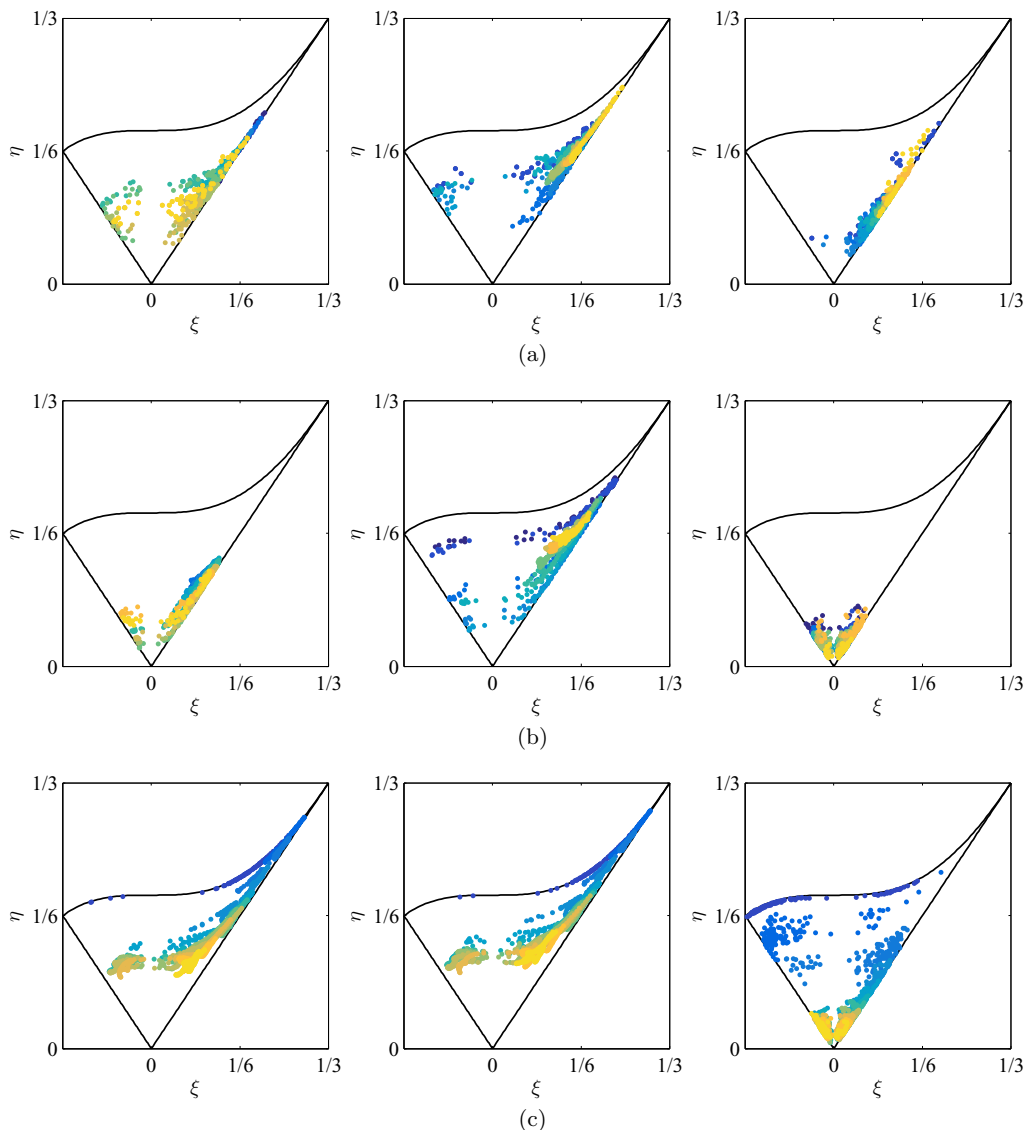
FIG. 16. Lumley's triangle composed with invariants derived from $\overline{u_i u_j}$ (left), $\overline{\overset{\circ}{u_i}\overset{\circ}{u_j}}$ (center), and $\overline{\hat{u_i}\hat{u_j}}$ (right). In each case, the threshold of $F_{\mathrm{int}} = 0.5$ is used. (a) Wind turbine wake $x/D = 0.5$, $N_r = 149$, (b) wind turbine wake $x/D = 6$, $N_r = 36$, and (c) channel flow DNS, $N_r = 115$.

the data suggest that low-order descriptions of the flow "flatten" turbulence, moving from fully three-dimensional states toward two-component turbulence. Three-dimensional turbulence requires three principle stresses for complete description. In contrast, a two-component turbulence field requires only two principle stresses, the orientation of which vary with location.

The complimentary effect is observed for the isotropic contribution to the flow. Invariants for isotropic contributions $\hat{\eta}$ and $\hat{\xi}$ are compared in the right column of Fig. 16. For representations of the flow using intermediate and high-rank POD modes, the invariants tend toward the isotropic condition, where $\hat{\eta} = \hat{\xi} = 0$. In the channel flow, there are points that contradict the tendency of invariants to decrease, located in the near-wall region. Areas where $\hat{\eta}$ and $\hat{\xi}$ indicate *less* isotropic flow coincide with locations where turbulent shear stresses are null near the wall. In both of the
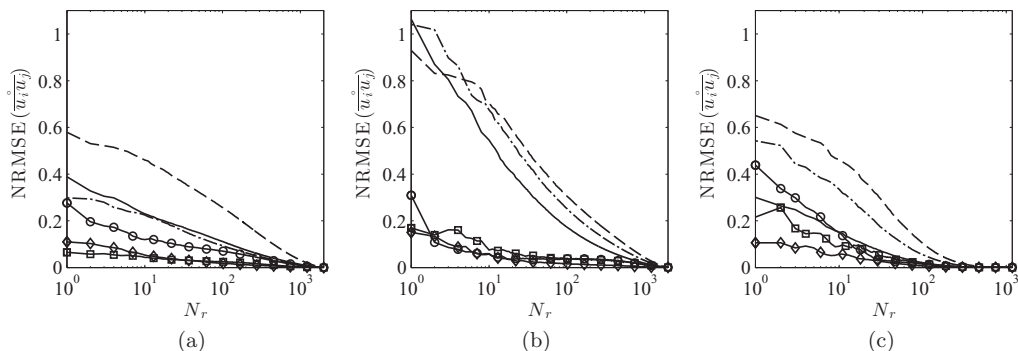
FIG. 17. NRMSE associated with reconstructed Reynolds stress tensor as a function of number of basis modes. In all subfigures, $\overline{uu}$ solid black lines, $\overline{vv}$ dashed lines, $\overline{ww}$ dash-dot lines, $-\overline{uv}$ circles, $-\overline{uw}$ diamonds, $-\overline{vw}$ squares. (a) Wind turbine wake, $x/D = 0.5$, (b) wind turbine wake, $x/D = 6$, and (c) channel flow DNS.

sampled measurement windows from the wind turbine wake, $\hat{\eta}$ and $\hat{\xi}$ are everywhere smaller in magnitude than η and ξ. Decreasing the threshold exaggerates the anisotropy seen in $\mathring{\eta}$ and $\mathring{\xi}$ while relaxing the distortion seen in $\hat{\eta}$ and $\hat{\xi}$. In using a truncated basis of POD modes for low-order models, retaining only a small number of modes greatly reduces the complexity of the resulting model. However, severe reductions of the basis leads to cases where the turbulence becomes identically one- or two-dimensional, shown analytically in the Appendix.

D. Error propagation via basis truncation

An important consideration in gauging the quality of a low-order description of the turbulence field is the accuracy of the reconstructed stresses. In the following analysis, the normalized root-mean-square error (NRMSE) of Reynolds stresses, invariants and anisotropy factors are considered according to

$$\text{NRMSE}(\mathring{g}) = \frac{\sqrt{\overline{(g - \mathring{g})^2}}}{\max(g) - \min(g)}, \tag{17}$$

where g is a reference quantity from the full statistics, $\mathring{g}$ is the quantity derived via low-order description, and the root-mean-square error is normalized by the span of g.

Figure 17 shows the NRMSE of the components of the Reynolds stress tensor as a function of the number of modes used in the description N_r. In the near wake of the wind turbine model [Fig. 17(a)], a truncated modal basis shows greatest error for $\overline{vv}$ regardless of the number of modes included. The near wake shows the most consistent behavior of all the cases; for all points of truncation of the POD basis, the normal stresses demonstrate greater error than the shear terms, and a rough proportionality is maintained between the errors.

The far wake in Fig. 17(b) shows considerably different behavior, wherein the normalized RMS error for normal stresses is far greater than that for the shear stresses. The far wake is the most isotropic among the studied cases, and the span of the normal stresses used to normalize the errors of $\overline{u_i \mathring{u_i}}$ are quite small. Additionally, because the shear terms contribute more significantly to the anisotropy tensor accounting for structures favored by low-rank POD modes, they reconstruct much faster than normal stresses. As the anisotropic features come out of the POD basis first, characteristic features of the shear terms are visible with as few as two modes. In the wake data, the spanwise normal stress is associated with large structures captured by POD. Spanwise homogeneity leads to decreased magnitudes of $\overline{ww}$ and low-rank POD modes fail to accurately reconstruct the spanwise normal stress.

Each data set indicates that the NRMSE is greatest for the normal stresses, with the exception of the channel flow in Fig. 17(c), which shows $\text{NRMSE}(\overline{u\mathring{v}}) > \text{NRMSE}(\overline{u\mathring{u}})$. Error of the streamwise or
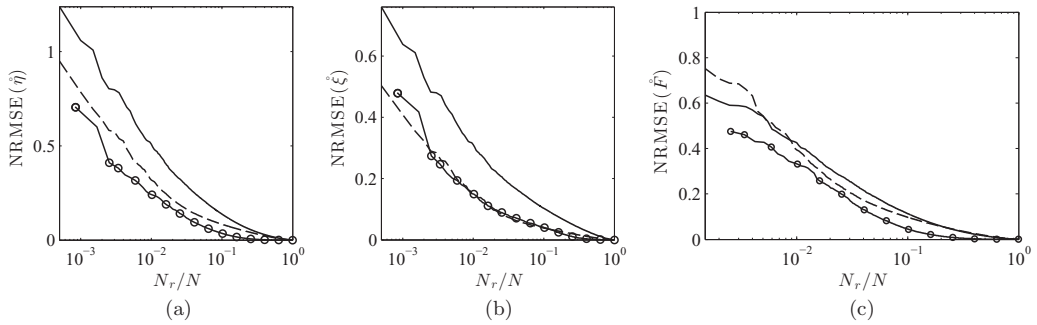
FIG. 18. Turbulence anisotropy error by basis truncation, N_r. Mode numbers are normalized by the total number of modes, N. Lines are $x/D = 0.5$ (solid lines), $x/D = 6$ (dashed lines), and the channel flow DNS data (circles). (a) Normalized error of $\mathring{\eta}$, (b) normalized error of $\mathring{\xi}$, and (c) normalized error of equivalent anisotropy factor.

wall-normal shear stress falls below that of the streamwise normal stress after $N_r = 11$, just beyond the 50% energy threshold for the channel flow, but well below the anisotropy threshold. Normalizing the RMS errors demonstrates that error propagation through the POD basis is on the same order for the channel flow data as for the near wake data behind the wind turbine. Without normalization, the magnitudes of the stresses [and of NRMSE($\overline{u_i \mathring{u}_j}$)] for the channel flow are approximately three orders of magnitude smaller than for the wake data.

A similar gauge of quality for low-order descriptions compares the NRMSE of the invariants of the anisotropy tensor as functions of the number of modes included in the truncated POD basis. From the definition of η and ξ from the Reynolds stresses, it is expected that the error propagation of low-order descriptions of the invariants will be related to that of the turbulence stresses. The NRMSE of the anisotropy tensor invariants is quite similar for the channel flow and the far wake, but are both dominated by the normalized RMS error of the invariants in the near wake. For all data, the error of $\mathring{\xi}$ is less than the error of $\mathring{\eta}$. The NRMSE of the second invariant at $N_r = 1$ shows a maximum error of approximately 120% for $x/D = 0.5$ and a minimum error of approximately 75% for the channel flow. The equivalent anisotropy factor is computed from $\mathring{\eta}$ and $\mathring{\xi}$ and compared to original values, Fig. 18(c). Whereas the NRMSE of the anisotropy tensor invariants differ considerably for the near and far wake data, NRSME($\mathring{F}$) is quite similar between the two cases beyond the first few modes.

It is from the invariants of $\mathring{b}_{ij}$ that insight regarding the quality of the low-order descriptions of turbulence is gained. The invariants describe the relative balance of elements in the Reynolds stress tensor the state of turbulence in quantifiable terms. The NRMSE of the invariants provides a quantitative account of the ability of a low-order description to match statistics in the turbulence field. A visualization of the quality of low-order description is provided in Fig. 19, wherein the AIM of the channel flow is composed with increasingly complex descriptions of the flow. Increasing N_r leads the invariants to their original values, conforming to the reduction of NRMSE discussed above. Values of the normalized RMS error and the portion of energy accounted for in low-order descriptions are delineated in Table III.

A few points of interest arise from Fig. 19 regarding the ability of POD descriptions to represent the actual turbulence field. Figure 19(a) demonstrates that using a single mode (here accounting for 19% of the integrated TKE) is capable of formulating exclusively one-dimensional turbulence. Similarly, reconstruction with $N_r = 2$ [Fig. 19(b), 27.5% of the integrated TKE] is capable of reproducing identically two-dimensional turbulence only. It should be noted here that severe basis truncations ($N_r = 1$ and $N_r = 2$) still require three components of velocity to describe the turbulence field in the domain. The one- or two-dimensional turbulence is a local flattening only; while only one or two principle stresses are needed to describe the local stress field, their orientation changes in the domain. A global description of the turbulence still requires three velocity components. The
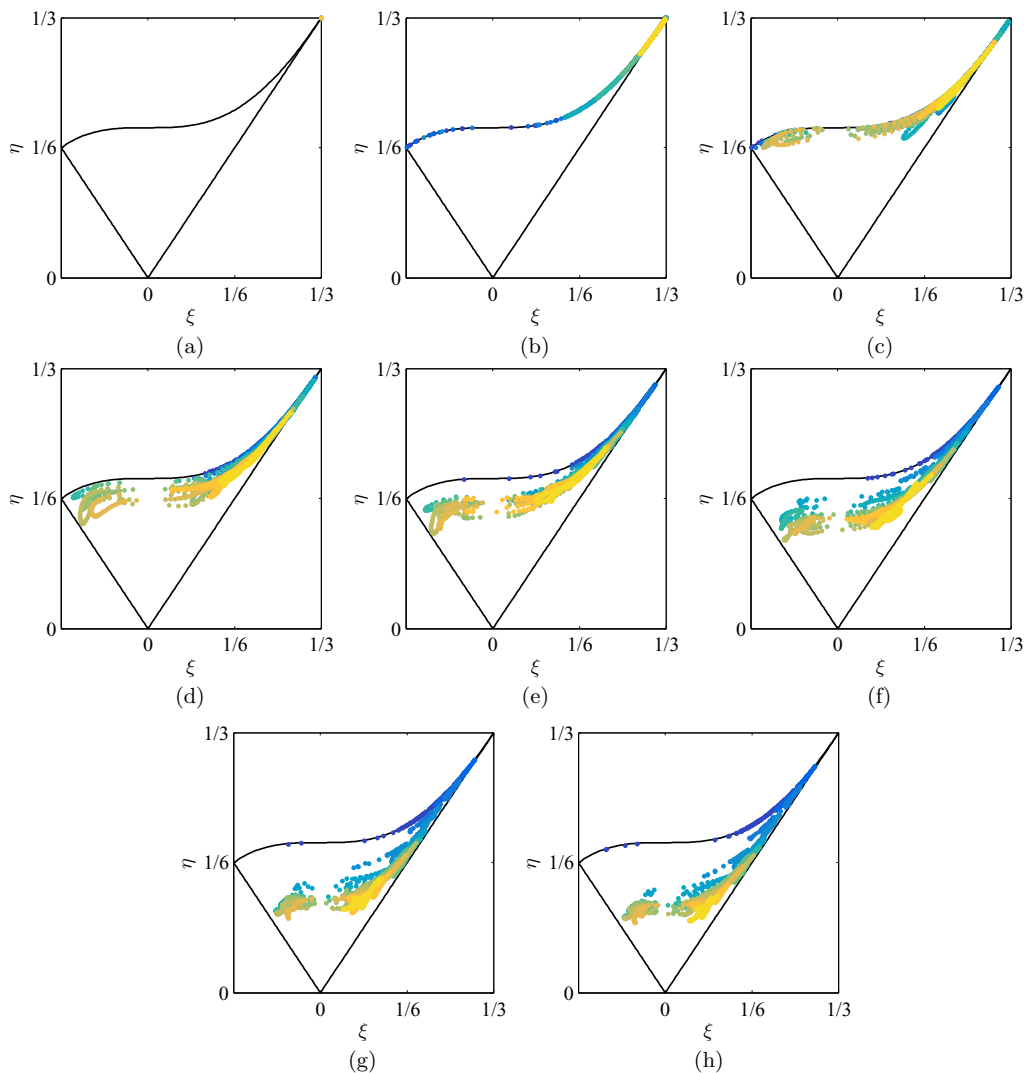
FIG. 19. Lumley's triangle for channel flow represented with increasing number of POD modes. See Table III for energy and NRMSE values for anisotropy factor and tensor invariants. (a) $Nr = 1$, (b) $Nr = 2$, (c) $Nr = 4$, (d) $Nr = 8$, (e) $Nr = 16$, (f) $Nr = 32$, (g) $Nr = 115$, and (h) original data.

reduction to one-and two-dimensional turbulence occurs identically for the wake data, although those Lumley's triangles are not shown.

Figures 19(c) through 19(f) show the AIM for invariants derived with models using $N_r = 4$, 8, 16, and 32 modes, accounting for 38.8%, 50.3%, 63.1%, and 75.9% of the turbulence kinetic energy, respectively. In each plot, the region of Lumley's triangle spanned by $\mathring{\eta}$ and $\mathring{\xi}$ converges toward the span described by η and ξ, provided in Fig. 19(h) for reference. In Figs. 19(c) and 19(d) the range of invariants is constrained to the upper region of the AIM as a result of the exclusion of the isotropic contribution to the Reynolds stress tensor. Increasing the truncation point to the threshold based on $\mathring{F}_{\text{int}} = 0.5$ [Fig. 19(g), $N_r = 115$], the invariants demonstrate behavior nearly identical the full statistics. The one- and two-dimensional behavior seen in the innermost region of the wall-bounded region is distinct from the three-dimensional turbulence seen in the outer layer. As more modes are included, the low-order description contains more isotropic background turbulence

TABLE III. Percentage kinetic energy and NRMSE values for anisotropy factor and tensor invariants for channel flow data with increasing number of POD modes. Data correspond to Figs. 19(a) through 19(g).

N_r	$(\mathrm{NRSME})(\mathring{\eta})$	$\mathrm{NRMSE}(\mathring{\xi})$	$\mathrm{NRMSE}(\mathring{F})$	ϵ
1	0.71	0.48	1.0	0.19
2	0.60	0.42	1.0	0.28
4	0.38	0.25	0.46	0.39
8	0.30	0.18	0.38	0.50
16	0.22	0.13	0.30	0.63
32	0.14	0.09	0.19	0.76
115	0.034	0.042	0.048	0.94

and the invariants move downward, toward their respective positions in the AIM described by η and ξ, Figure 19(h). As the POD representation tends toward the state derived statistically, the balance of terms $\overline{\mathring{u_i u_j}}$ more closely resembles that seen in $\overline{u_i u_j}$, a tendency reflected in $\mathring{\eta}$ and $\mathring{\xi}$.

E. Correction of the reduced-order flow description

A correction to the low-order flow descriptions arises from the observation that energy excluded from the truncated POD basis accounts for features that are both small and fairly homogeneous. This indicates that the energy excluded from the flow using $\overline{\mathring{u_i u_j}}$ may be considered as nearly constant background energy. Recent extensions of the double POD [31] corrected estimates of the Reynolds stresses by way of a constant coefficients used to push the magnitudes of each component toward the values seen in the full statistics. The basic formulation of such a correction is

$$\overline{u_i u_j} = C_{ij}\overline{\mathring{u_i u_j}}. \tag{18}$$

The correction coefficient C_{ij} is found through a minimization of the root-mean-square error err_{ij} between the statistical stress field and the corrected reduced-order model:

$$C_{ij} \ni \min\left[\frac{\sqrt{\langle(\overline{u_i u_j} - C_{ij}\overline{\mathring{u_i u_j}}|_{N_r})^2\rangle}}{\max(\overline{u_i u_j}) - \min(\overline{u_i u_j})}\right] = \min[\mathrm{NRMSE}(C_{ij}\overline{\mathring{u_i u_j}})]. \tag{19}$$

The correction applied to each component of $\overline{\mathring{u_i u_j}}$ is a constant that minimizes the NRMSE and effectively matches the magnitudes of the low-order descriptions to the statistical values. Correction of this type is attractive in that it is quite simple to derive and apply. However, there remains some error in the corrected stress fields arising from inhomogeneity in $\overline{\hat{u_i u_j}}$ that is ignored in the minimization of the error. As C_{ij} accounts for the difference between the turbulence field and its low-order description, it is necessarily a function of the number of modes used to compose $\overline{\mathring{u_i u_j}}$. Figures 20 and 21 show C_{ij} and the NRMSE between $\overline{u_i u_j}$ and $C_{ij}\overline{\mathring{u_i u_j}}$, respectively.

Seen in Fig. 20, the corrections associated with the normal stresses are larger in every case than those associated with the shear stresses. This is expected as the reconstruction of turbulence kinetic energy using POD is slower in the normal stresses than in the shear terms. The corrections $C_{2,2}$ and $C_{3,3}$ applied to the wall-normal and spanwise normal stresses are greatest in each case and for all POD truncations. C_{ij} falls off quickly for each case, where $C_{ij} < 2$ for all components beyond $N_r \approx 100$. An unanticipated result comes in the correction for the shear stress $-\overline{\mathring{v w}}$. This correction, unlike the others, is less than unity, which implies that the low-order description *over* estimates the energy using a truncated basis. In each of the data sets explored here, $\overline{vw}$ has the least energy of the Reynolds stress tensor. All other correction terms are strictly greater than unity, signifying that energy is excluded in the POD reconstruction.
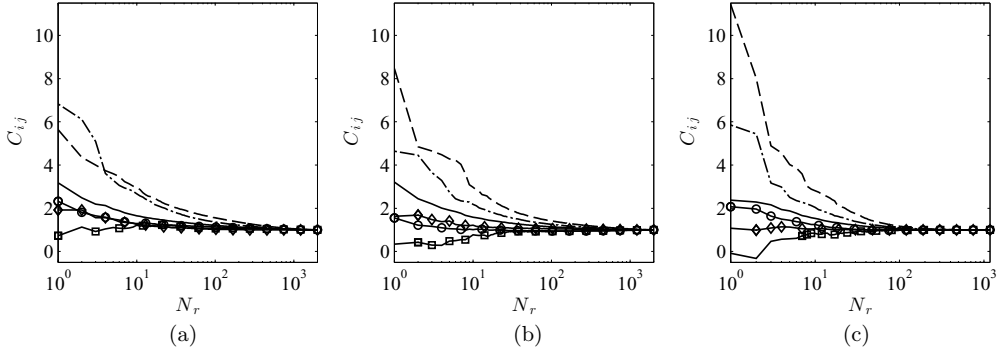
FIG. 20. Correction coefficient C_{ij} as a function of N_r. In all subfigures, $\overline{uu}$ solid black lines, $\overline{vv}$ dashed lines, $\overline{ww}$ dash-dot lines, $-\overline{uv}$ circles, $-\overline{uw}$ diamonds, $-\overline{vw}$ squares. (a) $x/D = 0.5$, (b) $x/D = 6$, and (c) channel flow.

Correction with C_{ij} leads to a significant reduction in NRMSE for all stresses and all cases. Figure 21 details the error of the corrected POD reconstructions according to the definition in Eq. (19). The maximum error for each case is associated with $C_{1,1}\overline{uu}$, similar to the error seen in the uncorrected low-order descriptions. The error with shear stresses is maximum for the $C_{1,2}\overset{\circ}{\overline{uv}}$ from the data located at $x/D = 0.5$ but falls off quickly to be less than 5% everywhere. Comparing the NRMSE($\overline{u_i u_j}$) to NRMSE($C_{ij}\overline{u_i u_j}$) indicates that truncation error is reduced by 30% for the near wake and channel flow data and about 55% for the far wake.

The correction factors shown in Fig. 20 and the associated errors shown in Fig. 21 indicate that there are notable gains in terms of accuracy of low-order descriptions of turbulence from simple corrections. Invariants derived from corrected low-order descriptions are denoted with a subscript c, as in $\overset{\circ}{\eta}_c$ and $\overset{\circ}{\xi}_c$. Application of C_{ij} to the low-order description reduces the NRMSE of the resulting anisotropy invariants by more than 50% for both η and ξ, see Fig. 22. Error associated with correction of this form is within 5% except in the near wake of the wind turbine. The correction is nonlinear and has effects in the overall balance of the modeled Reynolds stresses that in turn alter the behavior of the anisotropy tensor invariants. Each component of the correction tensor is defined to minimize the NRMSE of $\overline{u_i u_j}$ with the respective component of $\overline{u_i u_j}$. Energy is distributed to each component of the stress tensor at a different rate, and the corrections attempt to account for energy excluded from the truncated basis. A constant correction coefficient imperfectly assumes that energy is excluded homogeneously in the domain, leading to the NRMSE seen in Fig. 21.
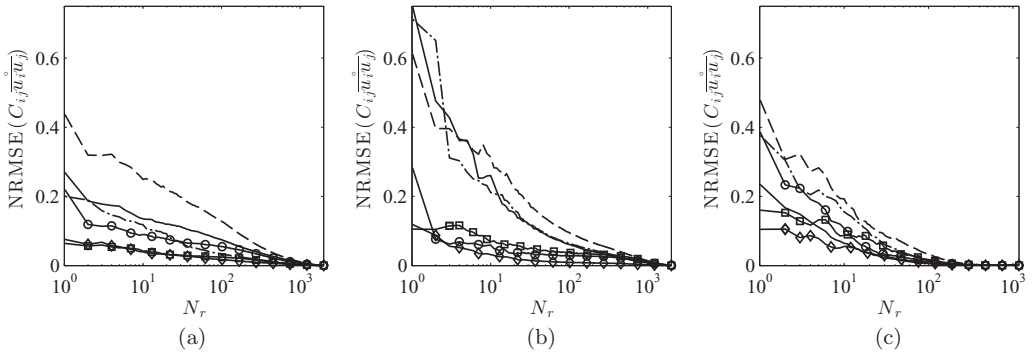

FIG. 21. NRMSE between $\overline{u_i u_j}$ and $C_{ij}\overline{u_i u_j}$. In all subfigures, $\overline{uu}$ solid black lines, $\overline{vv}$ dashed lines, $\overline{ww}$ dash-dot lines, $-\overline{uv}$ circles, $-\overline{uw}$ diamonds, $-\overline{vw}$ squares. (a) $x/D = 0.5$, (b) $x/D = 6$, and (c) channel flow.
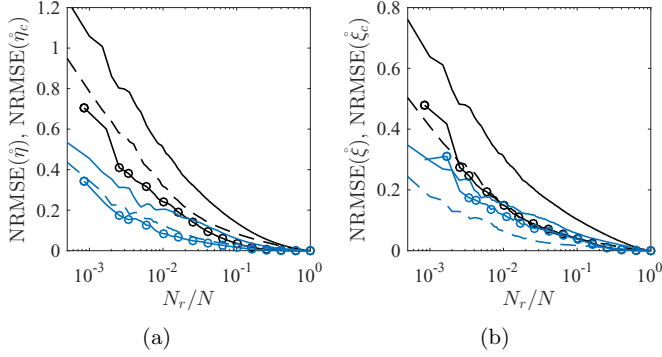
FIG. 22. NRMSE of anisotropy tensor invariants by mode number (black) compared to those after correction with C_{ij} (blue). Lines are $x/D = 0.5$ (solid lines), $x/D = 6$ (dashed lines), and the channel flow DNS data (circles).

Despite any remaining deviation from the original statistical field, it is encouraging to note that the proposed model correction can account for significant improvements in the behavior of the low-order invariants $\mathring{\eta}_c$ and $\mathring{\xi}_c$.

Corrected low-order invariants offer significant improvements to the equivalent anisotropy factor as well. Figure 23 compares the normalized RMS error of the invariants and the anisotropy factor before (black) and after correction (blue) with C_{ij}. After the correction, the equivalent anisotropy factor is not identically zero indicating that for severe basis truncations energy in the low-order description of turbulence is rebalanced. Stated otherwise, with the correction factor, three-dimensionality is reintroduced, where it was previously out of reach. These truncations were able to produce only one- and two-dimensional turbulence without correction. While reductions in error by 50% are certainly noteworthy by themselves, the accelerated convergence of $\mathring{F}_{\text{int},c}$ as compared to $\mathring{F}_{\text{int}}$ offers another hopeful result. The trends in Fig. 23(a) indicate that with the correction proposed above, the number of modes required to reach the $\mathring{F}_{\text{int}} = 0.5$ threshold is greatly reduced for all cases. After correction with C_{ij}, the anisotropy threshold is reached with as few as 8, 3, and 10 modes for the near wake, far wake, and channel flow (recall that before correction, $\mathring{F}_{\text{int}} = 0.5$ required 149, 36, and 115 modes).
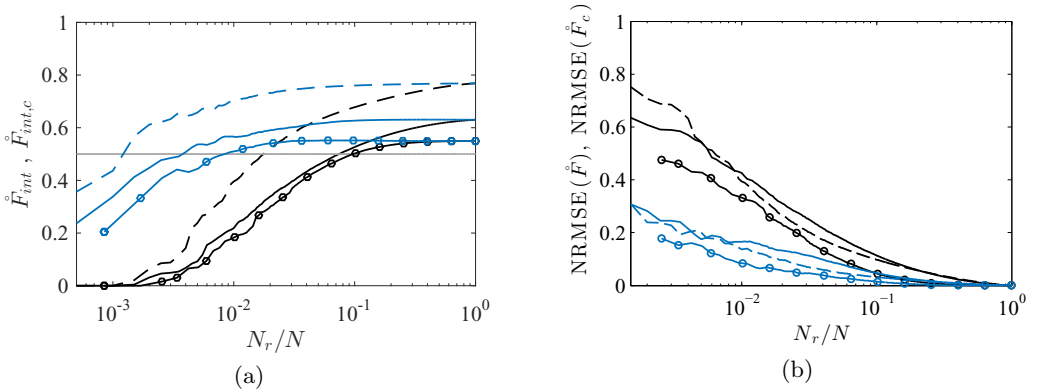
FIG. 23. Equivalent anisotropy factor $\mathring{F}_{\text{int}}$ (a) and the normalized RMS error of $\mathring{F}$ (b) by truncation point N_r, before (black) and after correction (blue). Mode numbers are normalized by their respective totals to allow even comparison.
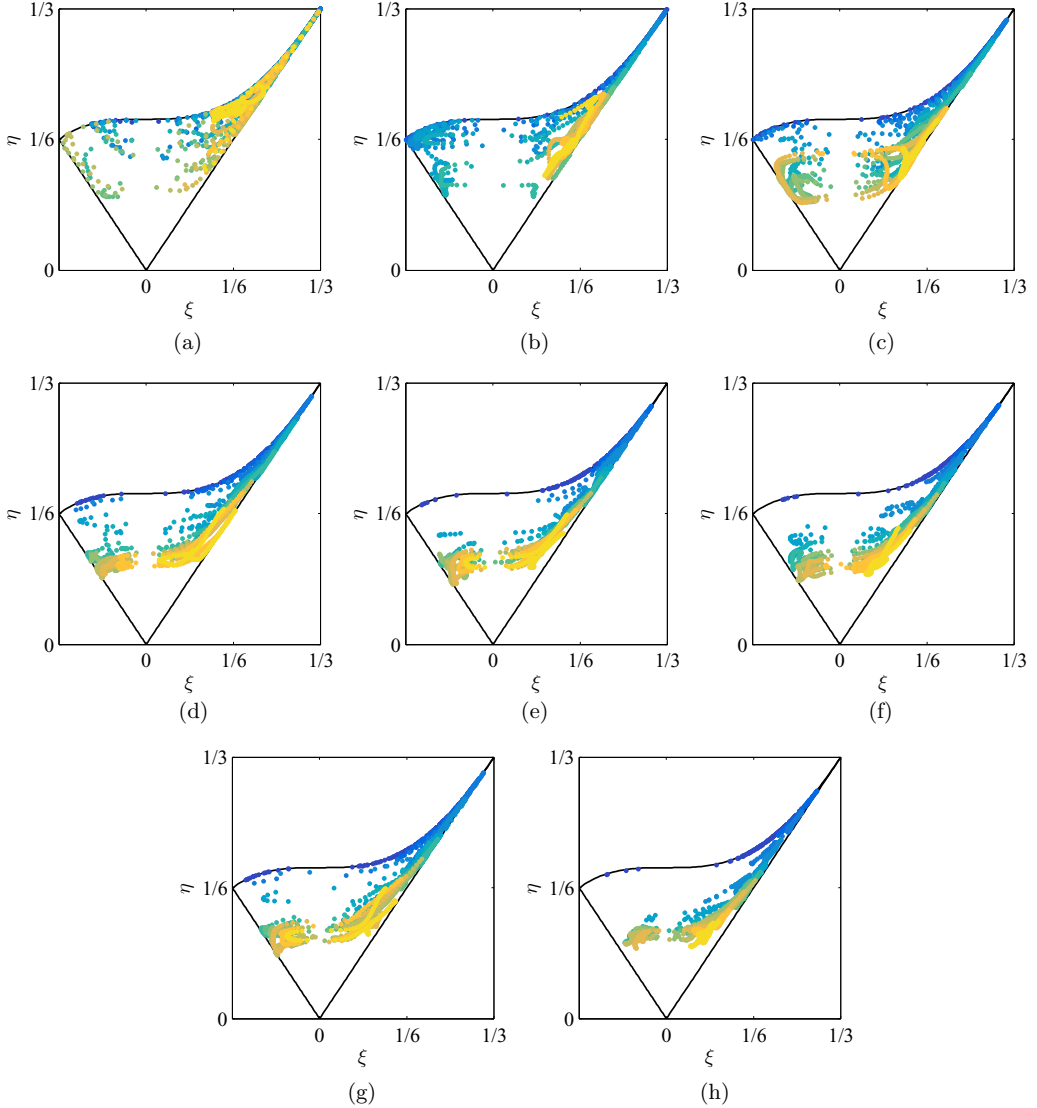
FIG. 24. Lumley's triangle for channel flow data after correction. Subfigure (g) shows the 10 mode approximation required to reach $\mathring{F}_{\text{int}} = 0.5$; (h) shows the full data for reference. (a) $N_r = 1$ corrected by C_{ij}, (b) $N_r = 2$ corrected by C_{ij}, (c) $N_r = 4$ corrected by C_{ij}, (d) $N_r = 8$ corrected by C_{ij}, (e) $N_r = 16$ corrected by C_{ij}, (f) $N_r = 32$ corrected by C_{ij}, (g) $N_r = 10$ corrected by C_{ij}, and (h) original data.

A visual demonstration of the improvements to the anisotropy tensor invariants is provided in Fig. 24. As indicated by $\mathring{F}_{\text{int},c}$, the AIMs with a $N_r = 1$ and $N_r = 2$ [Figs. 24(a) and 24(b)] are no longer constrained to one- and two-dimensional turbulence. Under correction, severe model reduction is capable of reproducing three-dimensional turbulence. As before, increasing the number of modes used in the low-order description leads to invariants that more closely match those of the original stress field. In each of the corrected AIMs, the minimum values of $\mathring{\eta}_c$ are nearly identical to those of η (Fig. 24), indicating that for at least some of the domain, the correct degree of isotropy is generated in the corrected turbulence fields. The two-dimensional behavior seen in the inner layer is unaffected by the correction and reconstructs accurately with a mode basis of any size. As it does for the Reynolds stress tensor, C_{ij} reduces the NRMSE between the anisotropy tensor invariants and their respective

low-order descriptions. Although behavior of the low-order invariants seen in Fig. 24 is much closer to η and ξ than the uncorrected versions, it is clear that error remains in the low-order description.

V. CONCLUSIONS

Proper orthogonal decomposition is a widely used analytical tool in the study of turbulent fluid flows. Large scales, expressing much of the turbulence kinetic energy, are accounted for by the first few POD modes and often describe the most important features of the flow. Because POD is able to efficiently describe the flow, the modes are used in reduced-order models such as in Galerkin projection and artificial neural-networks. Analysis of the invariants of the normalized Reynolds stress anisotropy tensor is a well-developed theoretical platform for characterizing the state of a turbulent flow. The second and third invariants are typically mapped against one another in Lumley's triangle, whose boundaries correspond to special states of turbulence which are used as limiting cases and boundary conditions. Mapping the invariants in Lumley's triangle provides insight into the balance of the Reynolds stress tensor and shed light on the nature of the flow.

The above work samples data from substantially different turbulent flow fields in an exploration of the anisotropic quality of low-order descriptions derived through truncated POD bases. Experimental data from a model-scale wind turbine wake are sampled very close to the model device, where the flow is intermittent and dominated by highly anisotropic turbulence, as well as the far wake, where the turbulence field is well-mixed and relatively isotropic. An alternate case is provided in the form of a sample of a direct numerical simulation of a fully developed channel flow. The innermost regions of the wall-bounded region of the flow are well-resolved in the data and have anisotropic properties conforming to the boundary conditions imposed on the simulation.

Application of POD to the data sets reveals the expected accumulation of energy expressed by the cumulative summation of POD eigenvalues. Low-order descriptions are made by truncating the basis of POD modes according to a 50% energy threshold, common practice in the use of POD. Although this threshold is arbitrary in terms of the error of the low-order description of the turbulence field, the 50% threshold is used frequently, presumably due to the comfortable equality of turbulence kinetic energy included and excluded from the resulting approximation of $\overline{u_i u_j}$. Mapping the propagation of normalized RMS errors between the low-order description and the statistically derived turbulence fields demonstrates that although a fair portion of the energy is excluded, the stress field represented with insignificant residual error. Composing the normalized Reynolds stress anisotropy tensor with the low-order description leads to new insights regarding the quality of the POD reconstructions.

An alternate truncation point for the POD basis is found by integrating the anisotropy factor of the low-order descriptions. As the lowest ranking POD modes account for the least isotropic turbulence structures, using only a few modes results in reduced values of $\mathring{F}_{int}$. A new threshold is introduced seeking the number of modes required to demonstrate $\mathring{F}_{int} = 0.5$, the midpoint between limiting values of F. Descriptions of the flow at the anisotropy factor threshold require more modes than the energy threshold, and the associate residual error is smaller. Lumley's triangles composed with the low-rank POD modes exhibit higher values of $\hat{\eta}$ and $\hat{\xi}$ than those derived from the full statistics due to the exclusion of any POD isotropic turbulence. Contrarily, the intermediate- and high-rank POD modes contribute much more to small-scale and homogeneous turbulence and result in smaller magnitudes of η and ξ, confirming that they express mainly isotropic turbulence structures.

A tensor of constant coefficients was defined to correct the magnitudes of each component of the low-order Reynolds stress tensor, minimizing the remaining NRMSE. Correction of this form assumes that the energy excluded from the POD approximation is homogeneously distributed isotropic turbulence kinetic energy. Residual NRMSE between the corrected POD approximation and the original statistics is approximately 25% lower than the uncorrected low-order description for the channel flow and approximately 30% lower for the wind turbine wake. The anisotropy tensor invariants show even greater reduction in residual error, nearly 50% of the uncorrected values. Most notably, correction with a tensor of constant coefficients effectively rebalances the magnitudes of the Reynolds stresses such that the invariants of the anisotropy tensor more closely resemble realistic

three-dimensional turbulence. In the cases of severe basis truncation, the POD descriptions are able to account for only one- or two-dimensional turbulence. Correction with constant coefficients enables the representation of three-dimensional turbulence for severe basis truncations. The correction further shifts the point where $\mathring{F}_{\text{int}} = 0.5$ by rebalancing the Reynolds stress tensor. After correction, the anisotropy threshold is reached using an order of magnitude fewer modes for all cases.

Through anisotropy tensor invariant analysis, the specific nature of the inaccuracy of data-driven low-order models arising from truncated POD basis is made evident. Specifically, it is shown that low-order models underestimate the magnitudes of the Reynolds stresses by excluding energy from the modal basis and simultaneously exaggerate the anisotropy of the flow. The proposed correction method accounts for both the exclusion of energy and the distortion of the anisotropy. Similarity apparent in the error propagation of POD models as well as correction tensor suggests that generalized corrections may be made for specific flow types or arrangements. Corrections explored above also make severe basis truncations accessible for modeling of three-dimensional turbulence.

APPENDIX: ANISOTROPY OF SEVERELY TRUNCATED BASES

The following development details the relationship of the POD mode basis to the invariants of the normalized Reynolds stress anisotropy tensor. According to the theory for the proper orthogonal decomposition, a low-order description of the Reynolds stress tensor may be composed as the linear combination of POD modes and their respective eigenvalues:

$$\overline{\mathring{u}_i \mathring{u}_j}_{N_r} = \sum_{n=1}^{N_r} \lambda^{(n)} \phi_{u_i}^{(n)} \phi_{u_j}^{(n)} = \begin{bmatrix} \sum_{n=1}^{N_r} \lambda^{(n)} \phi_u^{(n)} \phi_u^{(n)} & \sum_{n=1}^{N_r} \lambda^{(n)} \phi_u^{(n)} \phi_v^{(n)} & \sum_{n=1}^{N_r} \lambda^{(n)} \phi_u^{(n)} \phi_w^{(n)} \\ \sum_{n=1}^{N_r} \lambda^{(n)} \phi_v^{(n)} \phi_u^{(n)} & \sum_{n=1}^{N_r} \lambda^{(n)} \phi_v^{(n)} \phi_v^{(n)} & \sum_{n=1}^{N_r} \lambda^{(n)} \phi_v^{(n)} \phi_w^{(n)} \\ \sum_{n=1}^{N_r} \lambda^{(n)} \phi_w^{(n)} \phi_u^{(n)} & \sum_{n=1}^{N_r} \lambda^{(n)} \phi_w^{(n)} \phi_v^{(n)} & \sum_{n=1}^{N_r} \lambda^{(n)} \phi_w^{(n)} \phi_w^{(n)} \end{bmatrix}. \quad \text{(A1)}$$

POD lends energy to the reconstructed stresses equally, rather than distributing energy following the balance of terms in the original stress tensor. This leads ultimately to an alteration of the anisotropic state of the turbulence as shown in the invariants of $\mathring{b}_{ij}|_{N_r}$. Division by the turbulence kinetic energy is required to reach the normalized Reynolds stress anisotropy tensor. According to the low-order description above, the TKE is

$$\mathring{k}_{N_r} = \frac{1}{2} \text{tr}\left(\overline{\mathring{u}_i \mathring{u}_j}_{N_r}\right) = \frac{1}{2} \sum_{n=1}^{N_r} \lambda^{(n)} \phi_i^{(n)2}. \quad \text{(A2)}$$

1. $N_r = 1$

Limiting the POD basis to any single mode results in the simple description of the turbulence kinetic energy as

$$\mathring{k}_1 = \frac{1}{2}\left(\lambda^{(1)} \phi_u^{(1)2} + \lambda^{(1)} \phi_v^{(1)2} + \lambda^{(1)} \phi_w^{(1)2}\right). \quad \text{(A3)}$$

The turbulence kinetic energy is used to normalize the low-order description of the Reynolds stress tensor:

$$\mathring{b}_{ij,1} = \begin{bmatrix} \frac{\lambda^{(1)}\phi_u^{(1)2}}{2\mathring{k}_1} - \frac{1}{3} & \frac{\lambda^{(1)}\phi_u^{(1)}\phi_v^{(1)}}{2\mathring{k}_1} & \frac{\lambda^{(1)}\phi_u^{(1)}\phi_w^{(1)}}{2\mathring{k}_1} \\ \frac{\lambda^{(1)}\phi_u^{(1)}\phi_v^{(1)}}{2\mathring{k}_1} & \frac{\lambda^{(1)}\phi_v^{(1)2}}{2\mathring{k}_1} - \frac{1}{3} & \frac{\lambda^{(1)}\phi_v^{(1)}\phi_w^{(1)}}{2\mathring{k}_1} \\ \frac{\lambda^{(1)}\phi_u^{(1)}\phi_w^{(1)}}{2\mathring{k}_1} & \frac{\lambda^{(1)}\phi_v^{(1)}\phi_w^{(1)}}{2\mathring{k}_1} & \frac{\lambda^{(1)}\phi_w^{(1)2}}{2\mathring{k}_1} - \frac{1}{3} \end{bmatrix}. \tag{A4}$$

As a consequence of normalization of the first invariant of b_{ij}, defined as the trace of the tensor is zero:

$$\mathrm{tr}(\mathring{b}_{ij,1}) = \frac{\lambda^{(1)}\big(\phi_u^{(1)2} + \phi_v^{(1)2} + \phi_w^{(1)2}\big) - 2\mathring{k}_1}{2\mathring{k}_1} = 0. \tag{A5}$$

However, the second and third invariants are nonzero quantities. The second invariant η is related to the trace of the square of the normalized Reynolds stress anisotropy tensor. With a single POD mode, η is written

$$\mathring{\eta}_1 = \frac{1}{6}\left[\frac{4\mathring{k}_1^2 - 4\mathring{k}_1\lambda^{(1)}\big(\phi_u^{(1)2} + \phi_v^{(1)2} + \phi_w^{(1)2}\big) + 3\lambda^{(1)2}\big(\phi_u^{(1)2} + \phi_v^{(1)2} + \phi_w^{(1)2}\big)^2}{2\mathring{k}_1^2}\right]^{1/2}. \tag{A6}$$

Similarly, the third invariant of the normalized Reynolds stress anisotropy tensor, which describes the characteristic shape of the turbulence, is equated to the trace of the cube of normalized Reynolds stress anisotropy tensor. Using a single mode to describe the turbulence field, ξ evolves as

$$\begin{aligned} \mathring{\xi}_1 = \frac{1}{6\mathring{k}_1}\big[&-4\mathring{k}_1^3 + 6\mathring{k}_1^2\lambda^{(1)}\big(\phi_u^{(1)2} + \phi_v^{(1)2} + \phi_w^{(1)2}\big) \\ &- 9\mathring{k}_1\lambda^{(1)2}\big(\phi_u^{(1)2} + \phi_v^{(1)2} + \phi_w^{(1)2}\big)^2 + \tfrac{9}{2}\lambda^{(1)3}\big(\phi_u^{(1)2} + \phi_v^{(1)2} + \phi_w^{(1)2}\big)^3\big]^{1/3}. \end{aligned} \tag{A7}$$

In the above definitions for $\mathring{\eta}_1$ and $\mathring{\xi}_1$, the expressions may be simplified by substitution of the reduced-order turbulence kinetic energy $\mathring{k}_1$. In doing so, both invariants collapse identically to $\frac{1}{3}$ for the entire measurement domain. According to Lumley's triangle, $\eta = \xi = \frac{1}{3}$ corresponds to one-component turbulence. Thus, reduction of the POD mode basis to a single degree of freedom can represent only a single component of turbulence. The resultant turbulence needs not be fixed to any coordinate system and in fact changes direction relative to the original measurements; its alignment in space is expressed by the corresponding eigenvectors of $b_{ij,1}$.

2. $N_r = 2$

Increasing the mode basis used in the low-order descriptions of the turbulence field to $N_r = 2$ results in a similar but distinct development of the invariants of b_{ij}. With a basis of two POD modes, the low-order turbulence kinetic energy is written

$$\mathring{k}_2 = \tfrac{1}{2}\big[\lambda^{(1)}\big(\phi_u^{(1)2} + \phi_v^{(1)2} + \phi_w^{(1)2}\big) + \lambda^{(2)}\big(\phi_u^{(2)2} + \phi_v^{(2)2} + \phi_w^{(2)2}\big)\big]. \tag{A8}$$

The two terms in Eq. (A8) represent the respective contributions to the low-order TKE by the first and second POD modes. Note that each normal stress is multiplied by the respective eigenvalue, indicating that energy is distributed evenly to the u, v, and w components. The difference seen in the stresses is ultimately arbitrated by the POD modes rather than the eigenvalues. Using a basis of

two mode, the normalized Reynolds anisotropy tensor is written

$$
\mathring{b}_{ij,2} =
\begin{bmatrix}
\frac{\lambda^{(1)}\phi_u^{(1)2}+\lambda^{(2)}\phi_u^{(2)2}}{2\mathring{k}_2} - \frac{1}{3} & \frac{\lambda^{(1)}\phi_u^{(1)}\phi_v^{(1)}+\lambda^{(2)}\phi_u^{(2)}\phi_v^{(2)}}{2\mathring{k}_2} & \frac{\lambda^{(1)}\phi_u^{(1)}\phi_w^{(1)}+\lambda^{(2)}\phi_u^{(2)}\phi_w^{(2)}}{2\mathring{k}_2} \\[2mm]
\frac{\lambda^{(1)}\phi_u^{(1)}\phi_v^{(1)}+\lambda^{(2)}\phi_u^{(2)}\phi_v^{(2)}}{2\mathring{k}_2} & \frac{\lambda^{(1)}\phi_v^{(1)2}+\lambda^{(2)}\phi_v^{(2)2}}{2\mathring{k}_2} - \frac{1}{3} & \frac{\lambda^{(1)}\phi_v^{(1)}\phi_w^{(1)}+\lambda^{(2)}\phi_v^{(2)}\phi_w^{(2)}}{2\mathring{k}_2} \\[2mm]
\frac{\lambda^{(1)}\phi_u^{(1)}\phi_w^{(1)}+\lambda^{(2)}\phi_u^{(2)}\phi_w^{(2)}}{2\mathring{k}_2} & \frac{\lambda^{(1)}\phi_v^{(1)}\phi_w^{(1)}+\lambda^{(2)}\phi_v^{(2)}\phi_w^{(2)}}{2\mathring{k}_2} & \frac{\lambda^{(1)}\phi_w^{(1)2}+\lambda^{(2)}\phi_w^{(2)2}}{2\mathring{k}_2} - \frac{1}{3}
\end{bmatrix}.
\tag{A9}
$$

Normalization of $\overline{\mathring{u_i u_j}}|_2$ to arrive at $\mathring{b}_{ij,2}$ above is accomplished identically for that of $\overline{\mathring{u_i u_j}}|_1$. Consequently, the first invariant remains zero by definition:

$$
\mathrm{tr}(\mathring{b}_{ij,2}) = \frac{\lambda^{(1)}\big(\phi_u^{(1)2} + \phi_v^{(1)2} + \phi_w^{(1)2}\big) + \lambda^{(2)}\big(\phi_u^{(2)2} + \phi_v^{(2)2} + \phi_w^{(2)2}\big) - 2\mathring{k}_2}{2\mathring{k}_2} = 0.
\tag{A10}
$$

Higher invariants quickly become quite complicated to write in full. The second and third invariants now include terms involving the squares of POD mode components ($\phi_i^{(n)2}$) as well as cross-rank mode products ($\phi_i^{(1)}\phi_i^{(2)}$) and products of eigenvalues ($\lambda^{(1)}\lambda^{(2)}$). The two-mode definition of η is

$$
\begin{aligned}
\mathring{\eta}_2 = \frac{1}{6\mathring{k}_2}\Big\{ & 4\mathring{k}_2^2 - 6\mathring{k}_2\lambda^{(2)}\big(\phi_v^{(2)2} + \phi_w^{(2)2}\big) + 3\lambda^{(2)2}\big(\phi_v^{(2)2} + \phi_w^{(2)2}\big)\big(\phi_u^{(2)2} + \phi_v^{(2)2} + \phi_w^{(2)2}\big) \\
& + 3\lambda^{(1)}\lambda^{(2)}\big[-\phi_u^{(2)2}\big(\phi_v^{(1)2} + \phi_w^{(1)2}\big) + 2\phi_u^{(1)}\phi_u^{(2)}\big(\phi_v^{(1)}\phi_v^{(2)} + \phi_w^{(1)}\phi_w^{(2)}\big)\big] \\
& + 3\lambda^{(1)}\lambda^{(2)}\big[(\phi_v^{(1)}\phi_v^{(2)} + \phi_w^{(1)}\phi_w^{(2)})^2\big]\Big\}^{1/2}.
\end{aligned}
\tag{A11}
$$

Similarly, the two-mode definition of ξ is

$$
\begin{aligned}
\mathring{\xi}_2 = \frac{1}{6\mathring{k}_2^{2/3}}\Big\{ & 8\mathring{k}_2^2 - 18\mathring{k}_2\lambda^{(2)}\big(\phi_v^{(2)2} + \phi_w^{(2)2}\big) + 9\lambda^{(2)2}\big(\phi_v^{(2)2} + \phi_w^{(2)2}\big)\big(\phi_u^{(2)2} + \phi_v^{(2)2} + \phi_w^{(2)2}\big) \\
& + 9\lambda^{(1)}\lambda^{(2)}\big[-\phi_u^{(2)2}\big(\phi_v^{(1)2} + \phi_w^{(1)2}\big) + 2\phi_u^{(1)}\phi_u^{(2)}\big(\phi_v^{(1)}\phi_v^{(2)} + \phi_w^{(1)}\phi_w^{(2)}\big)\big] \\
& + 9\lambda^{(1)}\lambda^{(2)}\big(\phi_v^{(1)}\phi_v^{(2)} + \phi_w^{(1)}\phi_w^{(2)}\big)^2\Big\}^{1/3}.
\end{aligned}
\tag{A12}
$$

While complicated in full, the two invariants can be simplified using the definition of the two-mode TKE as done above for the single-mode approximation. Further, the invariants are related through an expression familiar to the analysis of turbulence anisotropy:

$$
\mathring{\eta}_2 = \big(\tfrac{1}{27} + 2\mathring{\xi}_2^3\big)^{1/2}.
\tag{A13}
$$

The relationship posed in Eq. (A13) defines the upper boundary of Lumley's triangle and describes two-component turbulence. As for the expansion of the invariants with a single POD mode, the orientation of the two resultant components is well described by the eigenvectors of $\mathring{b}_{ij,2}$.

The above demonstration indicates that in order to reproduce three-dimensional turbulence, a minimum of three POD modes are required to formulate the truncated basis. Using fewer modes results in either one- or two-component turbulence fields. Although each POD mode vectorial in nature containing three distinct components, they represent a single projection of the fluctuating velocity fields and thus a single degree of freedom. In the development including three or more POD modes, the definitions of η and ξ become arduously long and have not been included here.

---

[1] N. Aubry, R. Guyonnet, and R. Lima, Spatiotemporal analysis of complex signals: Theory and applications, J. Stat. Phys. **64**, 683 (1991).

[2] G. Berkooz, P. Holmes, and J. L. Lumley, The proper orthogonal decomposition in the analysis of turbulent flows, Annu. Rev. Fluid Mech. **25**, 539 (1993).

[3] J. L. Lumley, The structure of inhomogeneous turbulent flows, in *Atmospheric Turbulence and Radio Wave Propagation* (Nauka, Moscow, 1967), pp. 166–178.

[4] L. Sirovich, Turbulence and the dynamics of coherent structures part I: coherent structures, Q. Appl. Math. **45**, 561 (1987).

[5] M. Bergmann, L. Cordier, and J.-P. Brancher, Optimal rotary control of the cylinder wake using proper orthogonal decomposition reduced-order model, Phys. Fluids **17**, 097101 (2005).

[6] C. W. Rowley, Model reduction for fluids, using balanced proper orthogonal decomposition, Int. J. Bifurcation Chaos **15**, 997 (2005).

[7] K. Willcox and J. Peraire, Balanced model reduction via the proper orthogonal decomposition, AIAA J. **40**, 2323 (2002).

[8] L. Biferale and I. Procaccia, Anisotropy in turbulent flows and in turbulent transport, Phys. Rep. **414**, 43 (2005).

[9] J. Kim, P. Moin, and R. Moser, Turbulence statistics in fully developed channel flow at low Reynolds number, J. Fluid Mech. **177**, 133 (1987).

[10] K.-S. Choi and J. L. Lumley, The return to isotropy of homogeneous turbulence, J. Fluid Mech. **436**, 59 (2001).

[11] J. C. Rotta, Statistische theorie nichthomogener turbulenz, Z. Phys. **129**, 547 (1951).

[12] F. R. Menter, A. V. Garbaruk, and Y. Egorov, Explicit algebraic Reynolds stress models for anisotropic wall-bounded flows, in *Progress in Flight Physics* (EDP Sciences, 2012), Vol. 3, pp. 89–104.

[13] W. Rodi and G. Bergeles, Improved algebraic Reynolds stress model for engineering, in *Engineering Turbulence Modelling and Experiments-3* (Elsevier, 2012), p. 121.

[14] P. Mestayer, Local isotropy and anisotropy in a high-Reynolds-number turbulent boundary layer, J. Fluid Mech. **125**, 475 (1982).

[15] R. Smalley, S. Leonardi, R. Antonia, L. Djenidi, and P. Orlandi, Reynolds stress anisotropy of turbulent rough wall layers, Exp. Fluids **33**, 31 (2002).

[16] S. Leonardi, P. Orlandi, L. Djenidi, and R. A. Antonia, Structure of turbulent channel flow with square bars on one wall, Int. J. Heat Fluid Flow **25**, 384 (2004).

[17] W. D. Smyth and J. N. Moum, Anisotropy of turbulence in stably stratified mixing layers, Phys. Fluids **12**, 1343 (2000).

[18] R. Gómez-Elvira, A. Crespo, E. Migoya, F. Manuel, and J. Hernández, Anisotropy of turbulence in wind turbine wakes, J. Wind Eng. Ind. Aerodynam. **93**, 797 (2005).

[19] A. Jimenez, A. Crespo, E. Migoya, and J. Garcia, Advances in large-eddy simulation of a wind turbine wake, J. Phys.: Conf. Ser. **75**, 012041 (2007).

[20] N. Hamilton and R. B. Cal, Anisotropy of the Reynolds stress tensor in the wakes of wind turbine arrays in cartesian arrangements with counter-rotating rotors, Phys. Fluids **27**, 015102 (2015).

[21] S. G. Saddoughi and S. V. Veeravalli, Local isotropy in turbulent boundary layers at high Reynolds number, J. Fluid Mech. **268**, 333 (1994).

[22] A. A. Townnsend, Local isotropy in the turbulent wake of a cylinder, Aust. J. Chem. **1**, 161 (1948).

[23] R. A. Białecki, A. J. Kassab, and A. Fic, Proper orthogonal decomposition and modal analysis for acceleration of transient FEM thermal analysis, Int. J. Num. Methods Eng. **62**, 774 (2005).

[24] B. R. Noack, K. Afanasiev, M. Morzynski, G. Tadmor, and F. Thiele, A hierarchy of low-dimensional models for the transient and post-transient cylinder wake, J. Fluid Mech. **497**, 335 (2003).

[25] D. Rempfer, On low-dimensional Galerkin models for fluid flow, Theor. Comput. Fluid Dyn. **14**, 75 (2000).

[26] F. Tröltzsch and S. Volkwein, POD a-posteriori error estimates for linear-quadratic optimal control problems, Comp. Opt. Appl. **44**, 83 (2009).

[27] S. Pope, *Turbulent Flows* (Cambridge University Press, Cambridge, 2000).

[28] J. L. Lumley, Computational modeling of turbulent flows, Adv. Appl. Mech. **18**, 123 (1979).

[29] K. Hasselmann, Pips and pops: The reduction of complex dynamical systems using principal interaction and oscillation patterns, J. Geophys. Res. Atmos. **93**, 11015 (1988).

[30] N. Hamilton, M. Melius, and R. B. Cal, Wind turbine boundary layer arrays for cartesian and staggered configurations: Part I, Flow field and power measurements, Wind Energy **18**, 277 (2015).

[31] N. Hamilton, M. Tutkun, and R. B. Cal, Low-order representations of the canonical wind turbine array boundary layer via double proper orthogonal decomposition, Phys. Fluids **28**, 025103 (2016).

[32] J. Graham, M. Lee, N. Malaya, R. D. Moser, G. Eyink, C. Meneveau, K. Kanovand, R. Burns, and A. Szalay, *Turbulent Fhannel Flow Data Set* (Johns Hopkins University Press, Baltimore, 2013).

[33] Y. Li, E. Perlman, M. Wan, Y. Yang, C. Meneveau, R. Burns, S. Chen, A. Szalay, and G. Eyink, A public turbulence database cluster and applications to study Lagrangian evolution of velocity increments in turbulence, J. Turbulence **9**, N31 (2008).

[34] E. Perlman, R. Burns, Y. Li, and C. Meneveau, Data exploration of turbulence simulations using a database cluster, in *Proceedings of the 2007 ACM/IEEE Conference on Supercomputing* (ACM, 2007), p. 23.

[35] T. Mücke, D. Kleinhans, and J. Peinke, Atmospheric turbulence and its influence on the alternating loads on wind turbines, Wind Energy **14**, 301 (2011).

[36] N. Hamilton, H. Suk Kang, C. Meneveau, and R. B. Cal, Statistical analysis of kinetic energy entrainment in a model wind turbine array boundary layer, J. Renewable Sustainable Energy **4**, 063105 (2012).

[37] R. B. Cal, J. Lebrón, L. Castillo, H. S. Kang, and C. Meneveau, Experimental study of the horizontally averaged flow structure in a model wind-turbine array boundary layer, J. Renewable Sustainable Energy **2**, 013106 (2010).

[38] L. P. Chamorro and F. Porté-Agel, Turbulent flow inside and above a wind farm: A wind-tunnel study, Energies **4**, 1916 (2011).